Cell Reports

Article

Eicosapentaenoic acid reprograms cerebrovascular metabolism and impairs repair after brain injury, with relevance to chronic traumatic encephalopathy

Graphical abstract

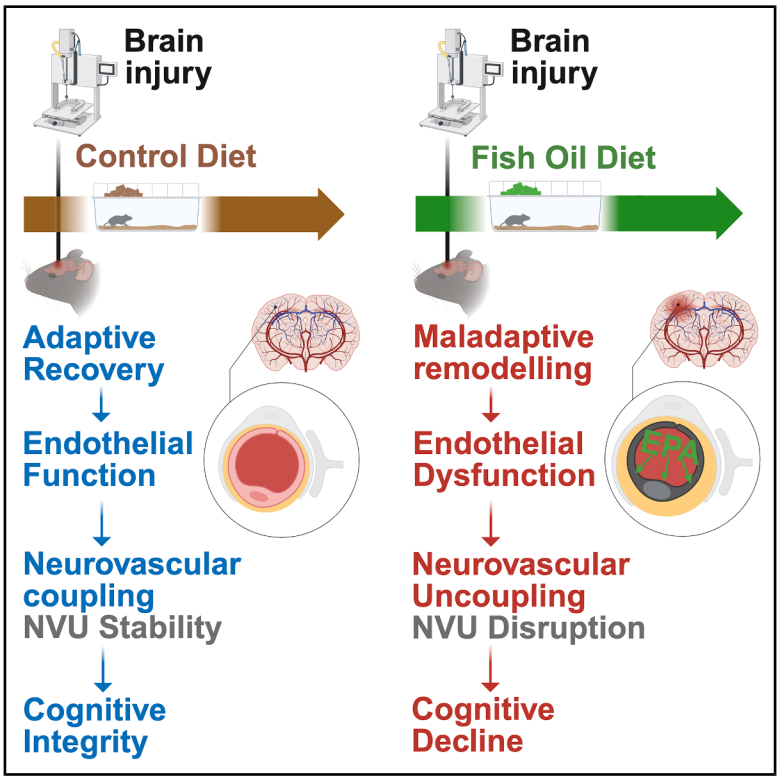

Authors

Eda Karakaya, Burak Berber, Onur Eskiocak, ..., Adviye Ergul, Semir Beyaz, Onder Albayram

Correspondence

beyaz@cshl.edu (S.B.), albayram@musc.edu (O.A.)

In brief

Karakaya et al. demonstrate that sustained dietary EPA exposure unmasks a latent metabolic vulnerability in the brain after TBI, driving maladaptive neurovascular remodeling, tauopathy, and cognitive decline. These findings challenge the paradigm of universal omega-3 neuroprotection and highlight the importance of metabolic context in brain injury outcomes.

Highlights

- EPA exposure after TBI unmasks a latent cerebrovascular vulnerability
- EPA reprograms endothelial metabolism, impairing vascular repair and remodeling
- EPA-driven neurovascular instability promotes tauopathy and cognitive decline
- Findings reveal metabolic context as key to omega-3 effects in brain injury

Karakaya et al., 2026, Cell Reports *45*, 117135
April 28, 2026
https://doi.org/10.1016/j.celrep.2026.117135

CellPress

Cell Reports

CellPress
OPEN ACCESS

Article

Eicosapentaenoic acid reprograms cerebrovascular metabolism and impairs repair after brain injury, with relevance to chronic traumatic encephalopathy

Eda Karakaya,[1,2,12] Burak Berber,[1,3,12] Onur Eskiocak,[4,5,12] Jazlyn Edwards,[1] Randy Bent Barker,[1] Sarah Jamil,[1] Weiguo Li,[1] Yasir Abdul,[1] Maria Ericsson,[6] Thor Stein,[7,8,9] Ann McKee,[7,8,9,10] Adviye Ergul,[1,2] Semir Beyaz,[4,*] and Onder Albayram[1,2,11,13,*]

[1]Department of Pathology and Laboratory Medicine, ER-AL Neurovascular Protection Laboratory, Medical University of South Carolina, Charleston, SC 29425, USA
[2]Ralph H. Jackson Department of Veterans Affairs Medical Center, Charleston, SC 29425, USA
[3]Department of Biology, Eskisehir Technical University, Eskisehir 26555, Turkey
[4]Cold Spring Harbor Laboratory, Cold Spring Harbor, New York, NY 11724, USA
[5]Graduate Program in Genetics, Stony Brook University, New York, NY 11790, USA
[6]Electron Microscopy Laboratory, Department of Cell Biology, Harvard Medical School, Boston, MA 02115, USA
[7]Boston University Alzheimer's Disease and CTE Center, Boston University School of Medicine, Boston, MA 02118, USA
[8]Department of Neurology, Boston University School of Medicine, Boston, MA 02118, USA
[9]VA Boston Healthcare System, Boston, MA 02130, USA
[10]Department of Pathology and Laboratory Medicine, Boston University School of Medicine, Boston, MA 02118, USA
[11]Department of Neuroscience, Medical University of South Carolina, Charleston, SC 29425, USA
[12]These authors contributed equally
[13]Lead contact
*Correspondence: beyaz@cshl.edu (S.B.), albayram@musc.edu (O.A.)
https://doi.org/10.1016/j.celrep.2026.117135

SUMMARY

Repetitive mild traumatic brain injury (rmTBI) precedes chronic traumatic encephalopathy (CTE) and involves neurovascular dysfunction. Omega-3 polyunsaturated fatty acids (PUFA) are promoted as neuroprotective but their long-term effects after brain injury remain uncertain. We uncover a metabolic vulnerability associated with cerebral accumulation of eicosapentaenoic acid (EPA), a major PUFA derived from fish oil. In a fish oil diet model, EPA accumulates at baseline yet is selectively depleted after rmTBI, consistent with mobilization during injury-associated metabolic remodeling. This pattern coincides with matrix remodeling, endothelial degeneration, and impaired neurovascular function. Cortical transcriptomics indicate reduced angiogenic programs with increased fatty acid metabolism, and lipidomics links EPA to maladaptive lipid engagement. Mechanistic studies using metabolically adapted endothelial cells show that EPA selectively impairs reparative function. Analysis of postmortem CTE brain tissue reveals parallel vascular and metabolic gene expression changes, strengthening translational relevance. Together, these findings challenge the assumption of uniform omega-3 neuroprotection after brain injury.

INTRODUCTION

Traumatic brain injury (TBI), often referred to as a "silent epidemic," remains a leading cause of death and long-term disability worldwide, disproportionately affecting young adults and the aging population.[1–5] Although repetitive mild TBI (rmTBI) is often regarded as benign, mounting evidence indicates that even subclinical injuries can initiate a chronic neurovascular injury cascade that persists for decades,[6–10] substantially elevating the risk of chronic traumatic encephalopathy (CTE) and dementia.[11–20] Despite its prevalence and long-term impact, no effective therapeutic strategies exist to halt or reverse the cerebrovascular deterioration associated with rmTBI,[21,22] leaving affected individuals vulnerable to decades of progressive cognitive decline.[23,24] Recent studies highlight that the capacity for cerebrovascular recovery is not uniform, but instead depends on the coordinated actions of brain microvascular endothelial cells (BMVECs) and extracellular matrix (ECM) remodeling, which together play a central role in orchestrating post-TBI repair.[25,26]

The brain's vascular network, spanning over 600 kilometers in length, is a critical infrastructure for cerebral metabolism, oxygen delivery, and waste clearance.[27] Following TBI, this cerebrovascular system is particularly susceptible to injury, with up to 50% of long-term survivors exhibiting persistent cerebrovascular pathology.[28,29] Angiogenesis, defined as the formation of new vessels from existing capillaries, is a key regenerative response supporting tissue repair and maintaining neurovascular unit

(NVU) integrity.[8,30–34] This process is tightly regulated by a dynamic interplay between BMVECs, ECM composition, and local metabolic cues.[35] However, disruptions in endothelial energy metabolism or signaling pathways may interfere with vascular regeneration and could contribute to long-term dysfunction and neurodegenerative processes.[28–30,35–37] Understanding how these cellular and metabolic factors shape the regenerative response is critical for developing targeted interventions in brain injury.

Fish oil (FO)-derived n-3 polyunsaturated fatty acids (PUFAs), particularly eicosapentaenoic acid (EPA) and docosahexaenoic acid (DHA), are among the most widely used dietary supplements for supporting systemic and brain health.[38] Unlike DHA, which is a major structural component of neuronal membranes, EPA exhibits limited membrane incorporation and has been reported to influence cognitive outcomes under specific conditions, such as dietary imbalance or cofactor deficiency.[39,40] While n-3 PUFAs are broadly recognized for neuroprotective roles, some studies suggest that their effects may vary based on the balance of lipid species, exposure duration, and physiological context—particularly in settings involving inflammation or injury.[41–43] Although several studies have reported that omega-3 PUFAs may support vascular stability in certain contexts, others suggest that specific lipid mediators, including EPA and its derivatives, could modulate angiogenic responses in a dose- and context-dependent manner.[44–46] Nevertheless, the relationship between long-term omega-3 intake and cerebrovascular adaptation after brain injury remains incompletely understood, especially as dietary supplements become increasingly prevalent among individuals with neurological vulnerability.

To address this knowledge gap, we implemented a cyclic FO-supplemented dietary regimen designed to emulate intermittent omega-3 intake patterns, combined with a repetitive less-than-mild TBI (rlmTBI) model that does not produce long-term deficits in animals maintained on purified control diets.[47] This sensitized experimental framework enables the detection of subtle changes in cerebrovascular resilience that might otherwise remain obscured. Using an integrative approach spanning *in vivo*, *in vitro*, and human tissue analyses, we demonstrate that sustained EPA enrichment in the brain occurs without altering systemic metabolic parameters, and that this cerebral reservoir is selectively depleted after rlmTBI, indicating preferential EPA engagement during the injury response. Within this context, chronic EPA enrichment was associated with impaired vascular repair, neurovascular unit remodeling, and delayed cognitive recovery. In metabolically permissive cerebrovascular endothelial culture conditions designed to mimic the post-injury shift in substrate utilization, EPA, but not DHA, reduced angiogenic and wound repair capacity, weakened endothelial cohesion, and activated lipid-sensing pathways in a manner consistent with our cortical transcriptomic data. Finally, postmortem CTE tissue revealed convergent evidence of PUFA imbalance, vascular instability, and transcriptional signatures of altered fatty acid metabolism and suppressed angiogenesis in the disease-affected cortex. Together, these findings suggest that sustained EPA exposure represents a context-dependent metabolic vulnerability capable of compromising cerebrovascular resilience after brain injury.

RESULTS

Prolonged FO supplementation drives aberrant EPA accumulation, reveals a latent metabolic vulnerability following TBI

Long-chain n-3 PUFAs, particularly EPA and DHA, are widely recognized as critical regulators of neurovascular health and metabolic homeostasis.[38] Yet, despite their broad therapeutic appeal, the long-term consequences of sustained dietary n-3 PUFA enrichment on cerebral lipid metabolism remain unresolved. In our model, prolonged FO-derived n-3 PUFA intake led to a marked buildup of unesterified EPA in the brain under homeostatic conditions, and this pool was selectively reduced following repetitive mild injury, a pattern revealing a previously unrecognized form of lipid responsiveness. While this shift initially appears paradoxical in light of the long-standing view that cerebral fatty acid metabolism is relatively limited,[48–50] recent studies demonstrate that the healthy brain, particularly astrocytes, can oxidize fatty acids under specific conditions.[51,52] These insights suggest that the mobilization we observed reflects a context-dependent engagement of lipid reserves rather than a contradiction of baseline metabolic principles. Because long-chain PUFAs such as EPA and DHA are obtained predominantly from the diet, with only limited endogenous production via inefficient conversion from alpha linolenic acid,[53–56] we next examined how FO supplementation shapes circulating and cerebral pools of unesterified fatty acids under baseline and post-injury conditions.

To model chronic n-3 PUFA exposure under physiologically relevant conditions, we implemented a cyclic FO-supplemented high-fat diet (FO-Suppl. HFD) regimen in wild-type C57BL/6J mice beginning at two months of age. This diet alternated one day of FO-Suppl. HFD with two days of purified control diet, mimicking fluctuating human supplementation patterns. Control animals were maintained on a continuous purified diet. After 1 month on the diet, mice were subjected to either repetitive less-than-mild closed head injury (rlmTBI) or sham procedures, followed by continued dietary exposure for an additional 6 months to evaluate chronic post-injury consequences (Figures 1A and 1B). Importantly, the FO-Suppl. HFD did not affect total caloric intake, body weight, fasting blood glucose, or adiposity across dietary and injury conditions (Figures 1A–1F), confirming that systemic metabolic homeostasis remained intact throughout the study. However, quantification of unesterified (free) fatty acids via high-performance liquid chromatography-tandem mass spectrometry (HPLC-MS/MS) uncovered a striking cerebral lipid signature: EPA selectively and robustly accumulated in the brains of sham mice fed the cyclic FO-Suppl. HFD (Figures 1G and 1H), indicating a relative resistance to PUFA turnover under non-injured conditions. This accumulation was specific to EPA and not recapitulated by DHA, suggesting divergent metabolic fates of n-3 PUFAs in the brain. Notably, this reservoir was not static: in rlmTBI mice, cerebral EPA levels declined markedly over time (Figure 1I), while DHA levels remained unchanged, suggesting

CellPress
OPEN ACCESS

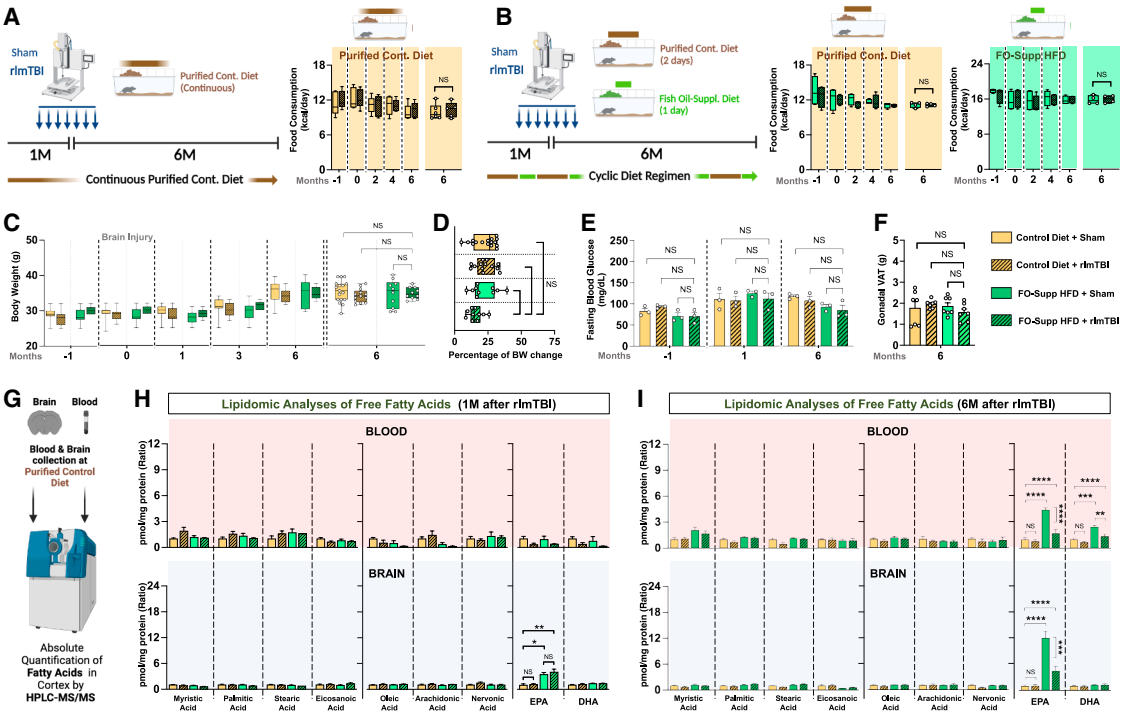

Figure 1. Chronic FO-Suppl. HFD promotes selective brain EPA accumulation and reveals a latent metabolic vulnerability following rImTBI

(A and B) Experimental design and dietary intake: wild-type C57BL/6J mice were randomized to a continuous purified control diet or a cyclic FO-Suppl. HFD at 2 months of age. After 1 month of dietary priming, mice underwent either rImTBI or sham procedures over 9 days. Diets were maintained for 6 months post-injury. Food consumption (kcal/day) remained consistent across groups, indicating FO-Suppl. HFD did not alter caloric intake or feeding behavior. $n = 5$ per group for food consumption.

(C–F) Systemic metabolic parameters: longitudinal assessment of body weight (C and D), blood glucose levels (E), and gonadal visceral adipose tissue mass (F) revealed no significant differences across dietary or injury conditions, confirming that FO-Suppl. HFD did not induce systemic metabolic disturbances. Each data point represents an individual animal; group sizes ranged from $n = 7$ to 14 mice per group.

(G–I) Targeted longitudinal free fatty acid analysis via HPLC-MS/MS in circulating blood and brain tissue at 1 and 6 months post-injury: at 1 month (H), FO-Suppl. HFD significantly increased EPA accumulation in the brain across both sham and rImTBI cohorts, with negligible changes in circulating EPA or DHA, suggesting selective cerebral retention of EPA under homeostatic conditions. By 6 months (I), circulating EPA and DHA levels were elevated in all FO-Suppl. HFD-fed mice, indicating systemic PUFA oversaturation. However, brain EPA levels in the FO-Suppl. HFD + rImTBI group were significantly reduced relative to sham, reflecting progressive depletion under chronic post-injury metabolic stress ($n = 3$–5 per group for lipidomic).

Data are presented as mean ± SEM. Statistical significance was determined using one-way or two-way ANOVA with Tukey's, Sidak's, or Dunnett's multiple comparisons post hoc tests, as appropriate. NS, not significant. $^{*}p < 0.05$, $^{**}p < 0.01$, $^{***}p < 0.001$, and $^{****}p < 0.0001$.

that injury perturbs selective PUFA retention. At 6 months post-injury, FO-fed TBI animals exhibited a significant reduction in cerebral EPA levels compared to FO-sham, accompanied by a downward shift in circulating EPA; however, plasma EPA levels in FO-fed TBI mice remained higher than in control diet groups. At the six-month time point, FO-fed mice also showed a modest increase in circulating DHA, whereas cortical DHA levels remained unchanged, consistent with the tightly regulated and relatively slow adjustment of brain DHA compared with the more dynamically responsive EPA pool. In contrast, DHA remained remarkably stable in both blood and brain, reinforcing the view that EPA is uniquely responsive to injury-driven metabolic shifts.

Together, these findings indicate that while prolonged FO supplementation leads to EPA accumulation under baseline conditions, cerebral EPA levels decline after rImTBI, suggesting a dynamic, injury-associated change in PUFA retention. Rather than serving as a passive neuroprotective reserve, EPA appears metabolically engaged in the brain's response to injury. Notably, although the FO-supplemented diet provided higher absolute levels of several saturated and monounsaturated fatty acids, these broader dietary differences did not produce proportional changes in the unesterified pools. EPA was uniquely elevated in both plasma and brain, underscoring the remarkable specificity of the metabolic response to dietary intervention. At the chronic post-injury stage, EPA levels in FO-supplemented TBI mice declined compared to FO-sham, reflecting metabolic engagement in the injured brain, yet remained substantially higher than in control diet groups, demonstrating a highly selective adaptation to both dietary intake and injury. Together, these patterns indicate that EPA availability is not simply dictated by systemic supply but instead reflects coordinated, injury-associated changes in EPA handling, reinforcing the view

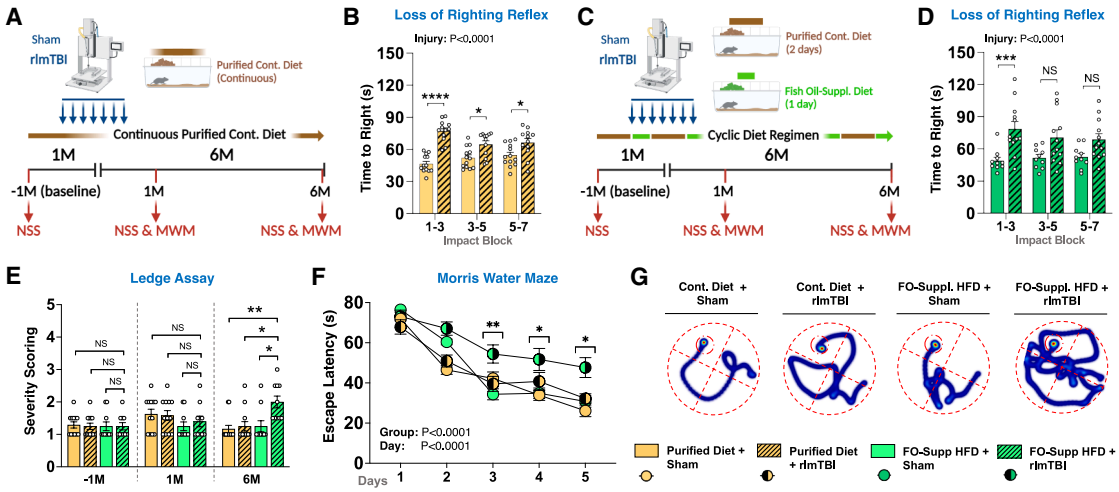

Figure 2. Chronic FO-Suppl. HFD selectively exacerbates long-term neurological dysfunction following rlmTBI

(A and C) Study design and behavioral timeline: schematic representation of the experimental paradigm showing the sequence of dietary intervention, rlmTBI induction, and longitudinal behavioral assessments at baseline (−1M), 1 month (1M), and 6 months (6M) post-injury in continuous control purified diet (A) and cyclic FO-Suppl. HFD (C) cohorts.

(B and D) Righting reflex recovery following rlmTBI. Both control purified (B) and FO-Suppl. HFD (D) rlmTBI groups exhibited significantly prolonged righting reflex recovery times compared to their respective sham controls ($p < 0.0001$), indicating comparable acute injury severity across dietary conditions.

(E) Sensorimotor performance (ledge assay): rlmTBI mice maintained on a control diet showed no sensorimotor impairments at either 1M or 6M post-injury. In contrast, FO-Suppl. HFD + rlmTBI mice exhibited significant motor deficits by 6M, indicating delayed-onset sensorimotor decline selectively in the FO-fed cohort.

(F and G) Cognitive performance (Morris water maze): at 6M post-injury, rlmTBI mice on a control diet performed comparably to sham animals across the 5-day spatial learning period.

(F) However, FO-Suppl. HFD + rlmTBI mice showed progressively worsening escape latencies.

(G) Day 2 session analysis revealed impaired learning efficiency and spatial navigation, further supported by heatmap visualizations of escape paths. Each data point represents an individual animal; group sizes ranged from $n = 10$ to $n = 13$ mice per group across experiments.

Data are presented as mean ± SEM. Statistical significance was determined using one-way or two-way ANOVA with Tukey's, Sidak's, or Dunnett's multiple comparisons post hoc tests, as appropriate. NS, not significant. *$p < 0.05$, **$p < 0.01$, ***$p < 0.001$, and ****$p < 0.0001$.

that EPA is the n-3 species most dynamically engaged by injury-driven metabolic shifts.

EPA-driven neurovascular instability triggers perivascular tauopathy and cognitive decline following TBI

Repetitive mild TBI (rmTBI) is a known precursor to CTE, yet the mechanisms by which early neurovascular disruption contributes to long-term cognitive decline remain incompletely understood. Whether this deterioration reflects the cumulative burden of injury alone or emerges from delayed, maladaptive metabolic shifts that remodel cerebrovascular function remains uncertain. Given the integral role of lipid metabolism in NVU maintenance, we hypothesized that prolonged dietary exposure to n-3 PUFAs, particularly EPA, may metabolically prime the NVU, and especially its endothelial compartment, for dysfunction following injury.

Using our established rlmTBI paradigm in combination with the cyclic FO-supplemented HFD, we next examined whether dietary background influenced the acute neurological suppression induced by injury. Recovery of the righting reflex, a standard index of transient post-impact neurological suppression rather than permanent loss of function, was significantly prolonged in rlmTBI mice compared with sham controls in both the purified control diet (Figures 2A and 2B; $p < 0.0001$) and FO-supplemented HFD groups (Figures 2C and 2D; $p < 0.0001$). Importantly, righting reflex latency did not differ between rlmTBI mice maintained on the purified control diet versus the FO-supplemented HFD, indicating that initial injury severity was equivalent across dietary conditions. However, long-term outcomes diverged between diet groups. Mice maintained on the purified control diet showed stable neurological scores and intact spatial learning over time, with no evidence of chronic deficits (Figures 2E–2G, S1A, and S1C). In contrast, FO Suppl. HFD + rlmTBI mice developed delayed behavioral abnormalities that became apparent at 6 months post-injury. Two-way repeated-measures ANOVA of the neurological severity scores revealed a significant group-by-time interaction, and Dunnett's post hoc testing identified higher scores at 6 months in the FO Suppl. HFD + rlmTBI animals compared with all other groups, whereas no differences were detected at baseline or 1 month (Figure 2E). Spatial learning performance in the Morris water maze was evaluated using a mixed effects model across the 5-day acquisition phase. This analysis showed significant effects of time and group, as well as a time by group interaction (time: $F[4,60] = 66.84$, $p < 0.0001$; group: $F[3,160] = 19.03$, $p < 0.0001$; and time × group: $F[12,160] = 2.33$, $p = 0.0088$). Bonferroni post hoc comparisons demonstrated that FO Suppl. HFD + rlmTBI mice exhibited longer escape latencies than all other groups on acquisition days 3–5 ($p < 0.05$–0.001), indicating

impaired spatial learning under conditions of sustained FO supplementation (Figures 2F, S1B, and S1D). Consistent with impaired acquisition, day 5 heatmaps demonstrated precise, target-directed swims in control groups, whereas FO-Suppl. HFD + rlmTBI mice showed continued reliance on perimeter-based searching, indicating an inability to form an effective spatial memory of the platform location (Figure 2G). Taken together, these findings indicate that chronic FO-supplemented high-fat feeding unmasks a delayed, diet-dependent vulnerability of neurobehavioral function after rlmTBI, whereas animals on the purified control diet retain long-term behavioral resilience.

Histopathological analysis linked these behavioral impairments to the emergence of perivascular tau pathology, a hallmark of early-stage CTE (Figure 3A). Immunostaining for hyperphosphorylated tau (AT8) revealed substantial accumulation in both neurons and perivascular compartments of the injured cortex in FO-Suppl. HFD-fed rlmTBI mice (Figures 3B–3D). Notably, AT8-positive signal showed prominent spatial association with lectin-labeled microvasculature, implicating vascular-associated compartments as a key site of tau aggregation. Consistent with this, complementary NeuN co-immunostaining confirmed increased neuronal AT8 accumulation in the same regions (Figure S2A), indicating that tau pathology extends beyond the vasculature while remaining closely coupled to microvascular domains. To further delineate the parenchymal correlates of delayed behavioral decline, we performed quantitative analysis of neuronal density, synaptic integrity, and microglial activation at 6 months post-injury. In FO-Suppl. HFD + rlmTBI mice, NeuN immunostaining revealed a mild but significant reduction in neuronal density compared to controls (Figure S2B). Notably, this selective neuronal vulnerability emerged in the context of preserved synaptophysin-integrated density across all groups (Figure S2C), indicating that presynaptic protein content and synaptic structure remained intact despite neuronal loss. Similarly, Iba1 immunoreactivity showed no significant differences, suggesting the absence of persistent microglial activation at this chronic stage (Figure S2D).

To assess the structural and functional integrity of the NVU, we conducted transmission electron microscopy (TEM) and measured neurovascular coupling via whisker-evoked cerebral blood flow responses. At 6 months post-injury, FO-Suppl. HFD-fed rlmTBI mice exhibited marked cerebrovascular remodeling, including narrowed vessel lumens (Figure 3F) and thickened basement membranes (Figure 3G), together with widespread endothelial degeneration characterized by cytoplasmic vacuolization (Figure 3H) and nuclear condensation (Figure 3I). Endothelial nuclei appeared hyperchromatic and condensed, contrasting with the diffuse euchromatin in controls, consistent with transcriptional arrest and metabolic stress within a structurally compromised NVU.[57,58] Importantly, these ultrastructural abnormalities were accompanied by functional impairment, as reflected by a blunted cerebral blood flow response to sensory stimulation (Figures 3J–3M), indicating disrupted neurovascular coupling. In contrast, assays of barrier integrity, including IgG extravasation and Prussian blue staining, did not show overt leakage at this chronic time point (Figures S1E–S1G). Together, these findings highlight a chronic neurovascular phenotype in which substantial basement membrane remodeling and endothelial injury coincide with impaired stimulus-evoked hemodynamic regulation, even when standard permeability readouts do not detect gross extravasation.

Given these structural and functional changes, we next assessed whether chronic FO-supplemented HFD influenced cerebral lipid peroxidation. Quantification of 4-hydroxynonenal (4-HNE) by immunohistochemistry and western blotting at 6 months post-injury (Figures S2E and S2F) revealed a trend toward increased 4-HNE levels in both FO-Suppl. HFD sham and FO-Suppl. HFD + rlmTBI groups compared to controls, although these differences did not reach statistical significance. This modest, non-significant increase suggests a subtle elevation in lipid peroxidation with prolonged omega-3 exposure; however, its contribution to chronic neurovascular dysfunction remains to be determined.

Together, these findings suggest that prolonged dietary EPA enrichment may influence neurovascular structure and function following rmTBI, potentially contributing to tauopathy and cognitive impairment over time. This pathophysiological sequence, characterized by endothelial degeneration within the NVU, basement membrane thickening, and impaired hemodynamic responses, occurs without overt blood-brain barrier (BBB) leakage, indicating a subclinical form of neurovascular dysfunction. These results suggest that sustained EPA exposure may contribute to cerebrovascular remodeling and could influence the brain's vulnerability to progressive decline, highlighting the importance of considering context when interpreting n-3 PUFA effects.

EPA reprograms cortical transcriptional responses and suppresses angiogenic signaling following TBI

To mechanistically dissect the transcriptional programs underlying EPA-induced neurovascular fragility, we performed RNA sequencing (RNA-seq) followed by weighted gene co-expression network analysis (WGCNA)[59] on injured cortical tissue from mice exposed to rlmTBI and chronic FO-Suppl. HFD. This systems-level approach identified discrete gene modules selectively altered in FO-Suppl. HFD + rlmTBI mice compared to all control conditions, including purified diet + sham, purified diet + rlmTBI, and FO-Suppl. HFD + sham. Among the 32,057 transcripts analyzed, hierarchical clustering revealed 30 eigengene modules, of which two, MEpurple (1,323 genes) and MEdarkred (743 genes), were significantly enriched ($p < 0.05$) in the FO-Suppl. HFD + rlmTBI group, representing a unique molecular signature of chronic PUFA exposure in the injured brain (Figures 4A and S3). Gene ontology analysis of these modules revealed widespread dysregulation of transcriptional programs critical for ECM homeostasis, angiogenic signaling, endothelial proliferation and migration, and lipid metabolic pathways, including fatty-acyl-CoA turnover (Figure 4B). Expression heatmaps and violin plots further demonstrated distinct transcriptional shifts across categories, such as ECM remodeling, angiogenesis, and fatty acid metabolism, alongside perturbations in solute carrier (SLC) transporters essential for brain endothelial nutrient exchange (Figures 4C–4G). Taken together, these findings suggest that chronic FO exposure post-TBI elicits a coordinated alteration in neurovascular repair mechanisms and metabolic adaptation. FO-Suppl. HFD + rlmTBI animals

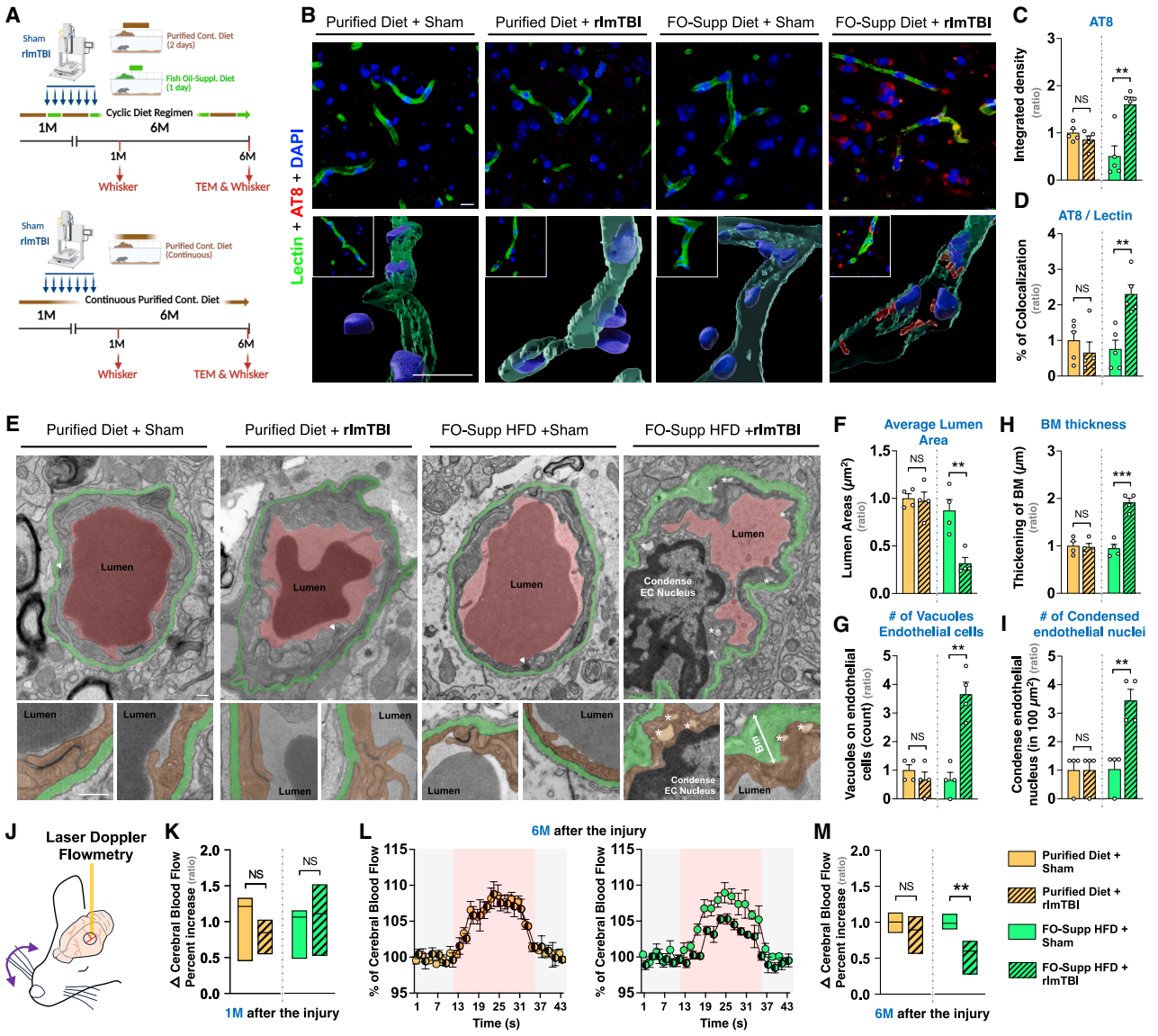

Figure 3. Chronic FO-Suppl. HFD exacerbates neurovascular pathology and impairs functional cerebrovascular responses following rImTBI

(A) Study design and experimental timeline: schematic outlining the sequence of dietary exposure, rImTBI induction, and longitudinal pathophysiological assessments at 1 and 6 months post-injury.

(B–D) Hyperphosphorylated tau accumulation at the neurovascular unit: representative confocal images and Imaris 3D reconstructions of cortical microvessels (B) demonstrate perivascular accumulation of hyperphosphorylated tau (AT8 immunoreactivity) in rImTBI mice fed a cyclic FO-Suppl. HFD. Scale bars, 20 μm. Quantification of AT8 integrated density (C) and AT8-lectin colocalization (D) confirmed significantly greater tau deposition in the FO-Suppl. HFD + rImTBI group, consistent with tauopathy localized to compromised NVU regions. $n = 5$ per group for perivascular histopathology.

(E–I) Ultrastructural deterioration of cerebrovascular integrity: transmission electron microscopy of cortical microvessels (E) revealed pronounced cerebrovascular remodeling in FO-Suppl. HFD + rImTBI mice, including reduced lumen area (F), increased endothelial vacuolization (G), basement membrane thickening (H), and nuclear condensation in BMVECs (I). White arrowheads indicate endothelial cells' normal euchromatic nuclei in control groups. The stars indicate the endothelial vacuolization. Scale bars, 250 nm. $n = 4$ per group for ultrastructural analysis.

(J–M) Delayed impairment of neurovascular coupling: representative laser Doppler flowmetry traces (J) depict the CBF response to whisker stimulation. Quantification at 1-month post-injury (K) revealed no significant changes in CBF dynamics across groups, indicating preserved early-phase neurovascular coupling. By 6 months post-injury (L and M), FO-Suppl. HFD + rImTBI mice exhibited a significant reduction in stimulus-evoked CBF response and ΔCBF percent increase, reflecting progressive neurovascular uncoupling and persistent cerebrovascular dysfunction. $n = 5$ per group for laser Doppler flowmetry.

Data are presented as mean ± SEM. Statistical significance was determined using one-way or two-way ANOVA with Tukey's, Sidak's, or Dunnett's multiple comparisons post hoc tests, as appropriate. NS, not significant. $^{*}p < 0.05$, $^{**}p < 0.01$, $^{***}p < 0.001$, and $^{****}p < 0.0001$.

CellPress
OPEN ACCESS

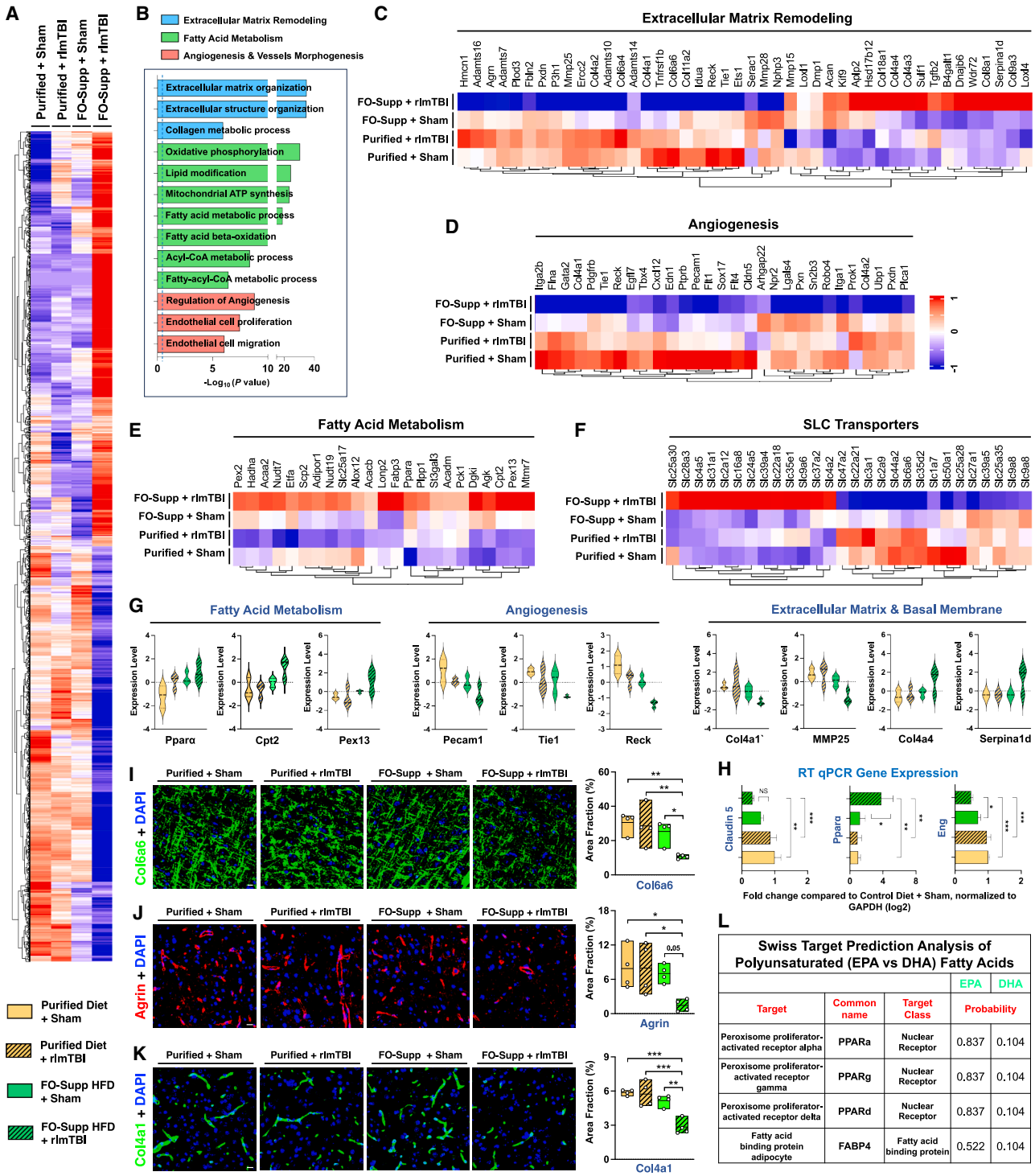

Figure 4. Chronic FO-Suppl. HFD disrupts gene networks governing maladaptive ECM remodeling, angiogenesis, and fatty acid metabolism following rlmTBI

(A) Transcriptomic divergence via WGCNA clustering: hierarchical clustering of 2,090 differentially expressed genes identified by WGCNA on RNA-seq data from injured cortical tissue. *Z*-score-normalized heatmap reveals a distinct transcriptional profile in FO-Suppl. HFD + rlmTBI mice that segregates from all other experimental conditions.

(B) Gene ontology terms associated with the FO-Suppl. HFD + rlmTBI group highlight significant disruptions in extracellular matrix organization, endothelial cell migration, angiogenic signaling, and fatty acid metabolic pathways, including β-oxidation and fatty-acyl-CoA turnover.

(legend continued on next page)

exhibited marked suppression of genes required for ECM structural integrity and vascular stability.

Critical ECM scaffolding components such as Agrn, Tie1, and Reck, key regulators of synaptic anchoring, vascular homeostasis, and matrix metalloproteinase (MMP) inhibition,[60–62] were significantly downregulated. Multiple α-collagen genes essential for basement membrane formation[63–65] (Col4a1, Col4a2, Col6a4, Col6a6, and Col11a2) were also repressed, alongside ECM turnover regulators from the Adamts protease family[66–68] (Adamts7, Adamts10, Adamts14, and Adamts16), indicating an impaired capacity for vascular remodeling. In contrast, profibrotic and matrix-depositing genes were upregulated, including Tgfb2 and Serpina1d, as well as fibrotic collagen isoforms (Col18a1, Col4a3, Col4a4, Col8a1, and Col9a3), suggesting maladaptive ECM remodeling and excessive matrix accumulation.

Key regulators of angiogenesis and endothelial stability were also broadly suppressed.[34,37] The expression of Cldn5, Pecam1, Itga1, and Itga2b, genes associated with endothelial junctions and adhesion, was significantly downregulated in the FO-Suppl. HFD + rlmTBI group. Additionally, pro-angiogenic signaling components, including Pdgfrβ, Cxcl12, and vascular basement membrane constituents Col4a1/Col4a2, were significantly downregulated, reflecting a blunted angiogenic response in the FO-Suppl. HFD + rlmTBI brain. Interestingly, classic pro-angiogenic ligands such as VEGFA, Angpt1/2, and FGF2 were not significantly altered. Instead, changes were enriched in structural, matrix-associated, and cytoskeletal genes, suggesting that EPA disrupts angiogenic competence via endothelial destabilization rather than direct inhibition of angiogenic signaling cascades.

Concurrently, transcriptomic analysis revealed a shift toward enhanced lipid metabolic programming.[69–72] Genes involved in fatty acid uptake and intracellular processing, including Ppara, Fabp3, Cpt2, Acaa2, Pex2, and Pex13, were significantly upregulated in the injured cortex of FO-Suppl. HFD-fed mice. Because these data derive from bulk cortical tissue, these genes cannot be ascribed to a single cell type, and many are expressed by multiple neural and vascular cells. However, increasing evidence suggests that endothelial cells utilize fatty acids for homeostasis and angiogenesis, and that fatty acid-binding proteins are implicated in endothelial function,[49,73] suggesting that alterations in lipid-handling pathways may influence both vascular and parenchymal metabolic states following injury.

Accordingly, the coordinated upregulation of these genes is consistent with broader cortical metabolic reprogramming that favors fatty acid engagement, potentially involving contributions from the neurovascular compartment. Rather than supporting reparative biosynthesis, this shift may reflect a maladaptive reallocation of metabolic resources in the post-injury environment. Parallel transcriptomic alterations were also observed in SLC transporter genes,[74–76] including Slc22a18, Slc28a3, Slc16a8, and Slc1a7, which regulate ion, nutrient, and metabolite flux across the BBB. Disruption of these transport systems may further compromise vascular and metabolic homeostasis following injury. To validate these transcriptomic trends, we performed immunofluorescence staining of injured cortical sections, which confirmed reduced expression of ECM-associated proteins *Col6a6*, *Agrn*, and *Col4a1* (Figures 4I–4K). Quantitative reverse-transcription PCR (RT-qPCR) analysis further supported transcriptional dysregulation, revealing downregulation of endothelial stability markers *Claudin-5* and *Endoglin (Eng)* alongside upregulation of *Ppara* (Figures 4H and S4), consistent with FO-Suppl. HFD-driven endothelial remodeling in the injured brain.

Lipidomic profiling over 6 months revealed sustained cerebral accumulation of EPA in sham animals maintained on the FO-Suppl. HFD. Following injury, however, EPA was selectively and substantially depleted in rlmTBI mice, despite continued dietary exposure, suggesting preferential mobilization and metabolic utilization of EPA under conditions of elevated energy demand. In contrast, DHA levels remained unchanged, highlighting a selective vulnerability in EPA handling. This depletion, following prior EPA enrichment, may reflect a metabolic priming effect that influences transcriptional responses after injury. To further elucidate the mechanism underlying EPA's selectivity, we performed in silico target prediction using SwissTargetPrediction. This analysis revealed high predicted binding probabilities for EPA to nuclear receptors, including peroxisome proliferator-activated receptors (PPARs) and fatty acid-binding proteins such as FABP4 (Figures 4L, S7, and S8). These findings suggest that EPA, but not DHA, may preferentially interact with transcriptional regulators of fatty acid metabolism, in a manner consistent with our transcriptomic data indicating modulation of fatty acid-responsive gene networks involved in vascular and metabolic adaptation to injury.

Together, these findings reveal that sustained dietary EPA exposure in the context of brain injury triggers a coordinated

(C–F) Pathway-specific transcriptional shifts: *Z*-score-normalized heatmaps illustrate widespread gene dysregulation in FO-Suppl. HFD + rlmTBI mice across four major categories: (C) ECM remodeling, (D) angiogenesis, (E) fatty acid metabolism, and (F) SLC transporters, underscoring global reprogramming of cerebrovascular repair machinery and metabolic substrate handling.

(G) Violin plots of key regulatory genes: quantification of representative genes from each disrupted category confirms selective transcriptional remodeling in the FO-Suppl. HFD + rlmTBI group, including fatty acid metabolism drivers (Ppara, Cpt2, and Pex13), angiogenesis-related genes (Pecam1, Tie1, and Reck), and ECM regulators (Col4a1, Col4a4, MMP25, and Serpina1d). n = 3–4 per group for transcriptomic analysis.

(H) RT-qPCR validation: quantitative PCR confirmed significant differential expression of *Claudin 5*, Ppara, and *Eng*, reinforcing FO-Suppl. HFD-induced impairments in endothelial integrity and vascular remodeling. n = 4 per group for RT-qPCR analysis.

(I–K) Immunofluorescence validation of maladaptive ECM remodeling: cortical staining confirmed downregulation of ECM components Col6a6 (I), Agrn (J), and Col4a1 (K) in FO-Suppl. HFD + rlmTBI mice, supporting a matrix environment prone to maladaptive remodeling. Scale bars, 20 μm. n = 4 per group for immunofluorescence analysis.

(L) SwissTargetPrediction analysis shows distinct target profiles for EPA and DHA. EPA strongly predicted binding to PPARα (probability = 0.84) and FABP4, whereas DHA exhibited weaker interactions with nuclear receptors, consistent with their divergent signaling effects (Figures S3 and S4).

Data are presented as mean ± SEM. Statistical significance was determined using one-way or two-way ANOVA with Tukey's, Sidak's, or Dunnett's multiple comparisons post hoc tests, as appropriate. NS, not significant. $^{*}p < 0.05$, $^{**}p < 0.01$, $^{***}p < 0.001$, and $^{****}p < 0.0001$.

transcriptomic shift characterized by impaired ECM organization, suppressed angiogenic and reparative signaling, upregulation of fatty acid oxidation pathways, and dysregulation of BBB transport systems. This molecular remodeling may reflect reduced metabolic flexibility and altered neurovascular homeostasis in the context of post-injury stress. By establishing a mechanistic link between EPA accumulation, injury-induced metabolic reprogramming, and failed recovery, these results challenge long-standing assumptions of n-3 PUFA benefit and identify a latent risk axis in lipid-based interventions. These findings contribute to a growing framework for understanding how dietary lipids interact with injury-adapted metabolism to shape long-term brain outcomes.

EPA utilization under permissive metabolic conditions impairs angiogenesis and endothelial integrity, recapitulating post-TBI cerebrovascular dysfunction

Angiogenesis is a cornerstone of neurovascular repair following TBI, requiring a coordinated interplay among endothelial cells, ECM remodeling, and adaptive energy metabolism.[35,77] In our *in vivo* model, prolonged exposure to a cyclic FO-Suppl. HFD led to progressive accumulation of EPA in the brain under homeostatic conditions; however, following TBI, EPA levels were selectively depleted, indicating preferential mobilization during the recovery phase and implicating EPA in sustained, injury-associated lipid remodeling. This shift was accompanied by prominent transcriptomic signatures of suppressed angiogenesis, ECM destabilization, and lipid metabolic reprogramming, suggesting that EPA exposure may predispose the vasculature to maladaptive remodeling and impair recovery following injury.

To mechanistically interrogate this vulnerability, we used BMVECs, the principal cellular mediators of angiogenesis and vascular stability, to assess whether EPA directly impairs reparative processes under conditions permissive for fatty acid engagement, thereby simulating the post-TBI metabolic milieu. Under physiological conditions, BMVECs rely predominantly on glycolysis for ATP production, reflecting an intrinsic metabolic preference for glucose over fatty acids due to their limited β-oxidation capacity.[50] However, following injury, elevated energy demands may trigger a compensatory shift in endothelial metabolism, leading to increased reliance on alternative substrates, such as fatty acids. To model this shift *in vitro*, we established a permissive metabolic environment in human-derived BMVECs (HBEC-5i) using AICAR, an AMP-activated protein kinase (AMPK) agonist that enhances mitochondrial substrate flexibility,[78] and L-carnitine, a cofactor that facilitates long-chain fatty acid transport into mitochondria. This approach simulates post-injury conditions that favor fatty acid engagement and enables targeted interrogation of the effects of EPA and DHA on cerebrovascular adaptation.

EPA, but not DHA, was associated with reduced angiogenic network formation under fatty acid-permissive conditions. In an endothelial tube formation assay, EPA (100 μM) combined with AICAR and L-carnitine (EPA + AC) significantly disrupted vascular network formation, reducing nodes (Figure 5B), junctions (Figure 5C), segments (Figure 5D), and meshes (Figure 5E), relative to vehicle and EPA-alone. In contrast, DHA (100 μM), with or without AICAR-carnitine, had no significant effect on angiogenic capacity (Figures 5A–5E), suggesting that EPA may interfere with angiogenic network formation under metabolic conditions that enhance fatty acid utilization, and highlighting a heightened endothelial sensitivity to EPA exposure in such contexts. The *in vitro* EPA and DHA concentrations (100 μM) were selected to reflect upper-range exposure conditions achievable through repeated supplementation or microdomain accumulation. Importantly, EPA alone did not affect angiogenesis in standard culture but impaired reparative dynamics only under permissive metabolic stimulation, underscoring a context-dependent mechanism. To investigate the molecular underpinnings of this dysfunction, we assessed the expression of claudin-5 and VE-cadherin, key structural proteins essential for endothelial cohesion, alongside the lipid-sensing nuclear receptor PPARα. EPA treatment under fatty acid-permissive conditions (EPA + AC), but not DHA, induced progressive downregulation of both claudin-5 and VE-cadherin, accompanied by upregulation of PPARα (Figures 5F–5H, S5, and S6). These findings suggest that EPA exposure under fatty acid-permissive conditions may influence endothelial phenotype and reduce angiogenic capacity.

To assess functional consequences, real-time impedance measurements using electric cell-substrate impedance sensing (ECIS) revealed a rapid decline in *trans*-endothelial electrical resistance (TEER) within 48 h of EPA + AC treatment, which continued to deteriorate through day 3 (Figure 5I), indicating compromised monolayer integrity and suppressed expansion. In a complementary ECIS-based wound healing assay, EPA + AC significantly delayed endothelial wound closure, while EPA alone had no detectable effect (Figure 5J). 3-(4,5-dimethylthiazol-2-yl)-2,5-diphenyltetrazolium bromide (MTT) assays further supported these findings, showing a time-dependent decline in BMVEC viability under EPA + AC conditions (Figure 5K).

These findings demonstrate that EPA, when metabolically engaged under conditions permissive to increased fatty acid flux, disrupts angiogenic signaling, destabilizes endothelial cohesion, and impairs reparative capacity, recapitulating key endothelial features of the neurovascular dysfunction observed *in vivo* following prolonged FO-supplemented HFD exposure in rlmTBI.

CTE brain reveals neurovascular and fatty acid metabolic reprogramming consistent with EPA-linked vulnerability

CTE is a progressive neurodegenerative disease linked to repetitive head trauma, but the role of chronic metabolic dysfunction, particularly in fatty acid handling, remains unresolved. Increasing evidence suggests that, beyond direct mechanical injury, metabolic inflexibility may contribute to cerebrovascular vulnerability. While our *in vivo* and *in vitro* models demonstrate that EPA is selectively mobilized under injury-induced metabolic demand, destabilizing endothelial architecture and impairing reparative signaling, it remains unclear whether the chronic disease state is characterized by similar or distinct forms of PUFA dysregulation. To address this, we examined postmortem brain tissue from neuropathologically confirmed CTE cases, aiming to determine whether signatures of maladaptive fatty acid metabolism

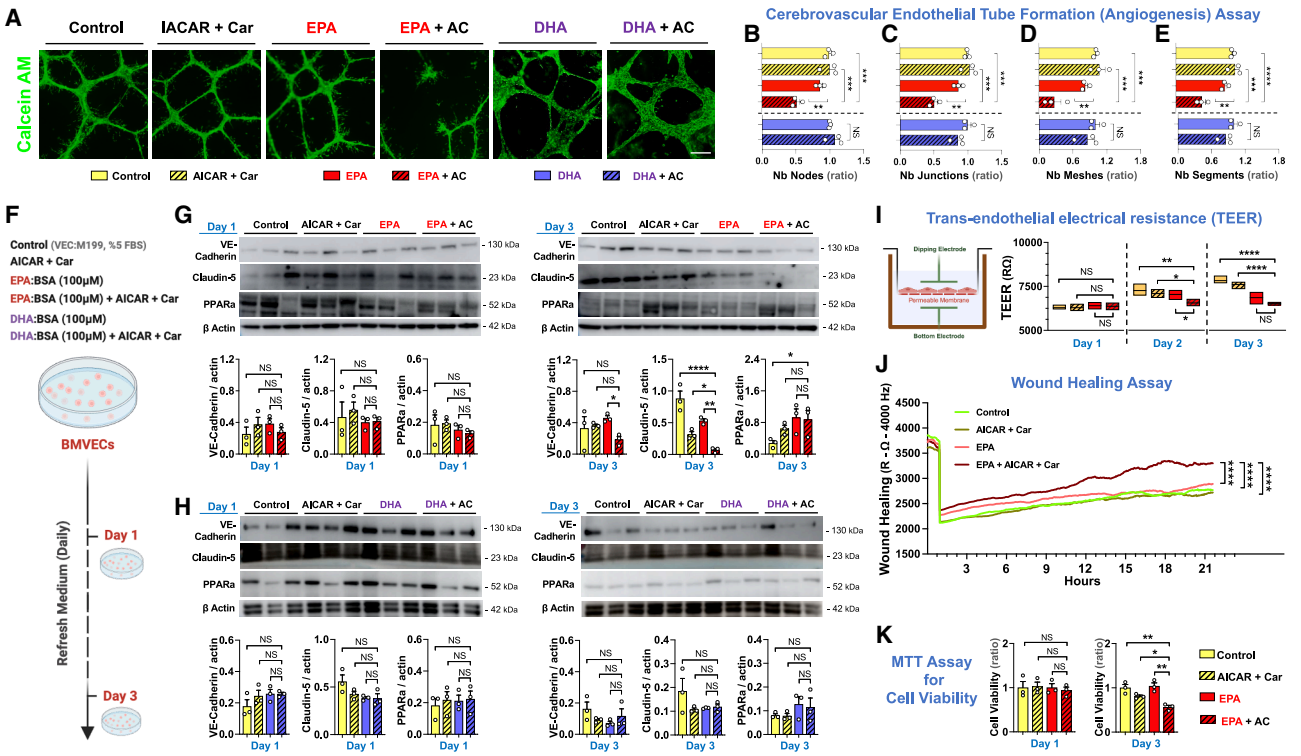

Figure 5. EPA-driven metabolic engagement disrupts endothelial integrity, angiogenesis, and regenerative capacity under conditions permissive to fatty acid utilization

(A–E) Impaired angiogenesis under EPA-driven metabolic conditions: cerebrovascular angiogenesis was assessed using a tube formation assay in human BMVECs. Representative calcein AM-stained images. Scale bars, 500 μm. (A) EPA, in combination with AICAR-carnitine (EPA + AC), markedly disrupted vascular network formation compared to control, AICAR-carnitine alone, EPA alone, DHA, or DHA + AC treatments. Quantification of angiogenic parameters, including node (B), junction (C), mesh (D), and segment (E) formation, demonstrated a significant reduction in angiogenic capacity only in the EPA + AC group.

(F–H) Western blot analysis of endothelial integrity and metabolic shift: protein expression of claudin-5, VE-cadherin, and PPARα was assessed on days 1 and 3. EPA + AC (G), but not DHA + AC (H), treatment led to a pronounced reduction in claudin-5 and VE-cadherin, indicating junctional destabilization, while concurrently upregulating PPARα, consistent with a shift toward fatty acid oxidation and metabolic reprogramming.

(I) *Trans*-endothelial electrical resistance (TEER) analysis of endothelial integrity: TEER measurements across a 72-h window revealed that EPA + AC treatment induced a progressive decline in barrier resistance, suggesting compromised endothelial stability and tight junction function. No comparable decline was observed in the other treatment groups.

(J) Delayed endothelial wound repair: an ECIS-based electrical wound healing assay showed that BMVECs treated with EPA + AC exhibited significantly delayed migration into the wound zone over 24 h, relative to all other groups. EPA alone did not impair migration, indicating the fatty acid-permissive metabolic context.

(K) Suppressed proliferation under permissive metabolic conditions: MTT assays revealed that EPA + AC treatment caused a significant, time-dependent decline in BMVEC viability on both days 1 and 3. This effect was not observed in control, EPA-alone, or DHA-treated groups, highlighting the metabolic specificity of EPA's detrimental impact. All *in vitro* experiments were performed using three independent biological replicates per condition.

Data are presented as mean ± SEM. Statistical significance was determined using one-way or two-way ANOVA with Tukey's, Sidak's, or Dunnett's multiple comparisons post hoc tests, as appropriate. NS, not significant. $*p < 0.05$, $**p < 0.01$, $***p < 0.001$, and $****p < 0.0001$.

and cerebrovascular dysfunction persist in the chronic phase of disease. This human analysis provides a translational context for interpreting our experimental findings and extends their relevance to clinical neurodegeneration.

We analyzed superior frontal cortex tissue from six neuropathologically confirmed CTE cases with a history of repetitive TBI (all < 75 years old) and six age- and sex-matched neurologically healthy controls (Figure 6A). Lipidomic profiling via HPLC-MS/MS revealed marked enrichment of PUFAs in CTE brains, including ~150% elevations in EPA and DHA and an 80% increase in arachidonic acid (AA) relative to controls (Figure 6C). Importantly, these differences were independent of body mass index (Figure 6B), suggesting intrinsic brain-specific alterations in fatty acid metabolism. This region-specific PUFA accumulation may reflect a metabolic disturbance that contrasts with the EPA depletion observed in our murine model—yet both patterns point to disrupted homeostatic PUFA handling in the context of traumatic stress. To determine whether this metabolic disturbance was accompanied by broader transcriptional remodeling, we performed RNA-seq on matched cortical tissue from confirmed CTE cases and controls. Differential expression analysis identified 2,678 significantly dysregulated genes (Figure 6D), spanning key biological domains including fatty acid metabolism, ECM remodeling, angiogenesis, and

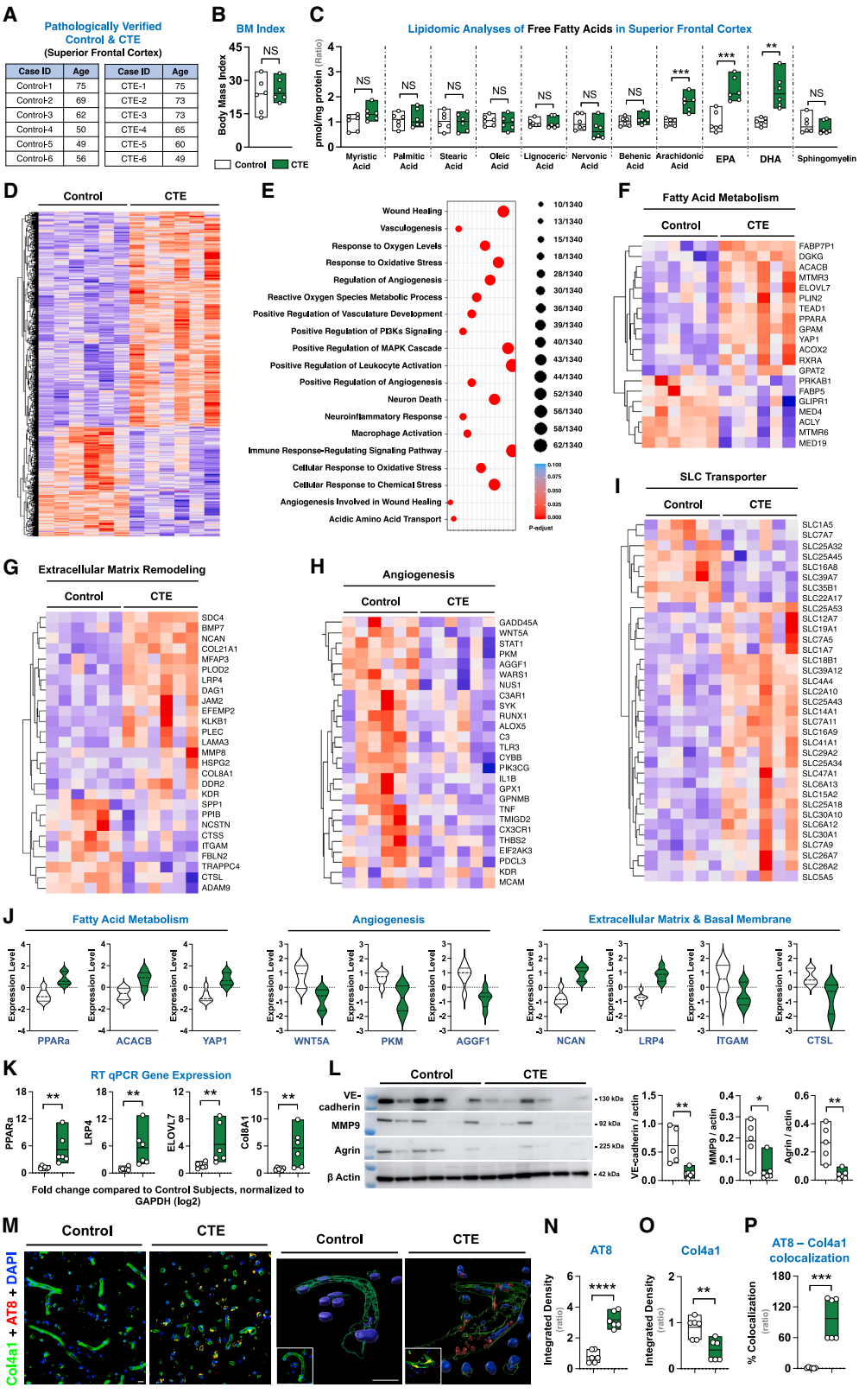

(legend on next page)

neuroinflammation (Figure 6E). Fatty acid metabolism pathways exhibited widespread disruption (Figure 6F), including differential regulation of genes governing oxidation (e.g., PRKAB1 and ACACB), elongation (e.g., ELOVL7), and desaturation. Downregulation of FABP5, ACLY, and MTMR6 suggested impaired lipid turnover and compromised energy-sensing capacity, whereas upregulation of PPARA, YAP1, TEAD1, and PLIN2 indicated increased peroxisomal lipid handling and lipid droplet formation, hallmarks of metabolic reprogramming. Concomitantly, ECM-related genes (Figure 6G) were markedly altered, including downregulation of AGRN and MMP9, critical for matrix remodeling and synaptic stability, and upregulation of COL8A1 and LRP4, suggesting pathological ECM restructuring. Angiogenesis-associated transcripts, including VE-cadherin (CDH5; Figure 6H), were significantly reduced, indicating impaired endothelial integrity. Perturbations in solute carrier (SLC) transporter expression (Figure 6I) indicated further disruption of nutrient and ion exchange at the blood-brain interface. Visualization through heatmaps and violin plots (Figure 6J) revealed consistent directional shifts in key gene clusters associated with fatty acid processing, vascular maintenance, and structural stability. qPCR (Figures 6K and S4) and western blot validation (Figures 6L and S7) confirmed differential expression of representative targets including PPARA, ELOVL7, LRP4, COL8A1, and VE-cadherin. These findings are consistent with the possibility that chronic PUFA accumulation in CTE may be associated with transcriptional remodeling, affecting vascular and metabolic pathways. In support of persistent neurovascular disruption, AT8 immunostaining revealed accumulation of hyperphosphorylated tau in both neuronal and perivascular compartments of affected cortical regions (Figures 6M–6P), a defining feature of disease progression and a spatial signature suggestive of NVU compromise. This pattern is consistent with a model where persistent vascular alterations may be involved in the progression of tau pathology in CTE.

The coordinated disruption of fatty acid metabolism, angiogenic signaling, and ECM remodeling defines a maladaptive axis in which impaired PUFA handling compromises vascular repair, destabilizes the neurovascular unit, and contributes to progressive neurodegeneration. While it remains unclear whether these alterations initiate disease or represent downstream adaptations to cumulative trauma, their reproducibility across *in vivo*, *in vitro*, and human systems highlights a shared and potentially targetable vulnerability. These insights raise the possibility that targeted modulation of cerebral PUFA metabolism could inform therapeutic strategies for TBI and related neurodegenerative conditions.

DISCUSSION

Long-chain n-3 PUFAs, particularly EPA and DHA, are widely regarded as neuroprotective dietary components. While DHA plays a well-established role in promoting membrane fluidity, synaptic resilience, and neurodevelopmental resilience,[79] the role of EPA in the injured brain remains less defined. Unlike DHA, EPA is minimally incorporated into neuronal membranes and has been associated with adverse cognitive and synaptic outcomes in preclinical models.[40,80] In this study, we directly challenge the prevailing assumption that all n-3 PUFAs confer uniform benefit across physiological states. Instead, our data reveal that sustained cerebral accumulation of EPA, under physiologically relevant dietary conditions, constitutes a latent metabolic liability that becomes unmasked in the context of repetitive mild TBI. This vulnerability appears to manifest through impaired vascular repair, endothelial stress, and maladaptive remodeling within the NVU, processes that may fundamentally redefine the cerebrovascular impact of dietary PUFAs and underscore the need for precision-guided strategies that account for context-dependent lipid metabolism in brain injury and disease.

Figure 6. Lipidomic and transcriptomic remodeling in the human CTE brain reveals metabolic reprogramming, impaired angiogenesis, and neurovascular destabilization

(A) Cohort overview: summary of neuropathologically verified human brain samples from the superior frontal cortex of patients with CTE and age- and sex-matched neurologically healthy controls.

(B and C) Lipidomic reprogramming in CTE cortex: despite no significant differences in body mass index (BMI) between groups (B), HPLC-MS/MS-based free fatty acid profiling (C) revealed profound PUFA accumulation in CTE brains, including marked elevations in EPA, DHA, and arachidonic acid, indicative of disrupted lipid homeostasis and sustained metabolic stress.

(D and E) Global transcriptional dysregulation in CTE: hierarchical clustering of 2,678 differentially expressed genes (D) from RNA-seq analysis of the superior frontal cortex reveals robust separation between CTE and control brains, highlighting widespread transcriptomic remodeling. Gene ontology enrichment analysis (E) identified significant perturbations in angiogenesis, neuroinflammation, wound healing, maladaptive ECM remodeling, and fatty acid metabolism.

(F–I) Pathway-specific transcriptional remodeling: heatmaps of *Z*-score-normalized gene expression values illustrate distinct regulatory shifts in the CTE across key pathways: fatty acid metabolism (F), extracellular matrix structure (G), angiogenesis (H), and SLC transporter function (I).

(J) Violin plots of pathway-specific gene expression: differential expression in CTE brains included upregulation of lipid regulators (PPARα, ACACB, and YAP1), ECM and vascular remodeling genes (LRP4, COL8A1, ITGAM, and CTSL), and angiogenic mediators (WNT5A, PKM, AGGF1), consistent with maladaptive vascular remodeling and metabolic reprogramming.

(K and L) Molecular validation of transcriptomic signatures: RT-qPCR (K) confirmed increased expression of PPARα, LRP4, ELOVL7, and COL8A1, reinforcing dysregulated fatty acid metabolism and maladaptive ECM remodeling in CTE. Western blot analysis (L) revealed downregulation of VE-cadherin, MMP9, and agrin, indicating compromised endothelial junctions and matrix degradation.

(M–P) Perivascular tauopathy in CTE cortex: immunofluorescence staining and Imaris 3D reconstruction (M) confirmed pathological accumulation of hyperphosphorylated tau (AT8) in the perivascular regions of the superior frontal cortex in CTE. Quantification of AT8 integrated density (N), Col4a1 expression (O), and AT8-Col4a1 colocalization (P) demonstrated enhanced perivascular tau deposition and NVU-specific degeneration. Each group comprised six subjects for each corresponding analysis ($n = 6$ CTE and $n = 6$ control).

Statistical significance was determined using unpaired two-tailed Student's *t* test (two-group comparisons) or one-way ANOVA with Tukey's multiple comparisons post hoc test (multi-group comparisons), as appropriate. $^{*}p < 0.05$, $^{**}p < 0.01$, $^{***}p < 0.001$, and $^{****}p < 0.0001$.

Across our complementary studies, we demonstrate that chronic EPA enrichment perturbs cerebrovascular fatty acid metabolism, impairs vascular repair, and contributes to progressive neurovascular dysfunction under conditions of elevated metabolic demand. In our cyclic FO-supplemented HFD model, designed to emulate real-world patterns of fish oil intake, EPA selectively accumulated in the brain without affecting peripheral metabolic parameters. Consistent with our lipidomic profiles, circulating EPA levels in FO-fed TBI mice were reduced relative to FO-fed sham mice, although they remained higher than in animals maintained on the purified control diet. Cerebral retention of EPA remained stable under homeostatic conditions but was rapidly mobilized following rlmTBI, indicating preferential substrate utilization in response to injury-adaptive metabolic conditions. While the FO-supplemented diet included both EPA and DHA, only EPA exhibited coordinated diet- and injury-related shifts in both circulation and cortex, whereas DHA remained stable in the brain despite modest increases in blood. This divergent pattern reflects the more conserved, phospholipid-bound nature of brain DHA and the more rapidly metabolized, beta-oxidized profile of EPA,[81–83] supporting that EPA, rather than DHA, acts as the principal mediator of injury-associated lipid reprogramming in our model.

Rather than conferring resilience, this metabolic shift coincided with impaired endothelial repair, destabilization of the NVU, and progressive vascular and cognitive decline. Notably, these effects were absent in animals maintained on continuous purified diets, underscoring a functional divergence in PUFA handling and injury response.[47] Structural and functional profiling revealed that FO-Suppl. HFD + rlmTBI mice exhibited pronounced thickening of the basement membrane, ultrastructural endothelial degeneration, and impaired neurovascular coupling, yet lacked detectable tracer extravasation, defining a latent cerebrovascular fragility state that may be missed by conventional permeability-focused assessments. This pattern is aligned with prior reports of persistent perivascular extracellular matrix remodeling in juvenile TBI models, where elevated fibronectin and perlecan expression were accompanied by reduced vessel diameter up to 6 months post-injury.[84] More broadly, converging preclinical and human data suggest that enduring NVU dysfunction, including structural remodeling and impaired cerebrovascular regulation, may evolve independently of BBB disruption and is sensitively detected by neurovascular coupling and cerebrovascular reactivity assessments.[85–87] These findings position our model within a growing recognition that cerebrovascular health must be evaluated beyond permeability metrics alone and that dietary PUFA context can shape long-term NVU vulnerability through mechanisms that involve both structural remodeling and physiological dysregulation. Although neuronal tau pathology and neuron loss were evident, there were no significant changes in presynaptic density or chronic Iba1 immunoreactivity, suggesting that neuronal vulnerability occurred independently of overt synaptic loss or persistent microglial activation.

In our study, we observed a non-significant, mild trend toward increased 4-HNE expression in FO-supplemented groups, suggesting that prolonged omega-3 exposure may modestly increase cerebral vulnerability to oxidative stress, particularly after repeated injury. The possibility that cumulative lipid peroxidation and ferroptotic signaling may contribute to delayed neurovascular dysfunction remains to be determined and represents an important direction for future investigation. Longitudinal studies will be essential to determine whether lipid peroxidation represents a transient response or a progressive driver of vascular compromise after brain injury.

While our current focus was on downstream endothelial phenotypes and transcriptional reprogramming, future work will investigate upstream mechanisms of EPA uptake and distribution, particularly the roles of fatty acid transport proteins, such as FATPs/SLC27 family members and FABPs, which may influence tissue-selective EPA delivery under stress conditions. Our *in vitro* model of metabolically adapted human BMVECs provided mechanistic validation. Under conditions permissive to increased fatty acid utilization, via AICAR-mediated AMPK activation and L-carnitine, EPA, but not DHA, suppressed angiogenic capacity, delayed wound closure, and downregulated key endothelial cohesion markers claudin-5 and VE-cadherin.

These structural and functional disruptions coincided with upregulation of lipid-sensing nuclear receptors, including PPARα, suggesting that EPA exposure under conditions permissive to fatty acid utilization reprograms endothelial behavior away from reparative competence. While prior studies have shown that omega-3 PUFAs, particularly DHA or mixed EPA/DHA formulations, can promote angiogenesis in developmental and retinal models,[88,89] these effects may not generalize to all tissues or physiological states. Our findings suggest that, in the context of adult brain injury, sustained EPA exposure may impair endothelial cohesion and regenerative capacity through mechanisms distinct from those seen in development. This apparent divergence likely reflects key differences in developmental versus injury-induced angiogenesis. Whereas retinal or embryonic models reflect tightly regulated vascular growth during development or early-life stress, post-traumatic cerebrovascular remodeling in the adult brain occurs alongside inflammation, ECM reorganization, and metabolic strain. Within this context, EPA disrupted angiogenic signaling and vascular stability, underscoring the need to interpret omega-3 PUFA effects through a lens of tissue specificity, lipid composition, and metabolic environment. To further explore potential receptor-level mechanisms, we conducted SwissTargetPrediction analysis, which revealed high predicted binding probabilities between EPA and PPARα and FABP4, key lipid sensors involved in transcriptional regulation, while DHA showed lower affinity for these targets. These predictions align with our transcriptomic data and will require future experimental validation (Figures S8 and S9).

Postmortem analysis of neuropathologically confirmed CTE brain tissue revealed molecular and metabolic features that converge with those observed in our experimental models. Lipidomic profiling of the superior frontal cortex demonstrated aberrant regional accumulation of EPA, DHA, and arachidonic acid, despite stable body mass index, indicating localized disruption of PUFA homeostasis. Transcriptomic analysis identified extensive gene dysregulation affecting pathways involved in fatty acid metabolism, ECM remodeling, angiogenesis, and neuroinflammation, including prominent upregulation of peroxisomal β-oxidation components and downregulation of

endothelial repair pathways. Protein-level and immunohistochemical validation revealed perivascular tau accumulation, downregulation of VE-cadherin, and overexpression of COL8A1, markers consistent with chronic vascular stress and maladaptive matrix remodeling.

Together, these multi-platform findings suggest that EPA, while often regarded as neuroprotective, may play a context-dependent role in shaping metabolic responses in the injured brain, thereby undermining cerebrovascular resilience through maladaptive engagement of endothelial lipid metabolism. Across complementary models, chronic EPA enrichment disrupted angiogenic signaling, destabilized endothelial cohesion, and promoted ECM remodeling, defining a mechanistic axis of vascular vulnerability in the post-injury setting. Rather than supporting adaptive energy metabolism, the elevated ACACB expression observed in both FO-supplemented HFD-fed rlmTBI mice and human CTE cortex may reflect a maladaptive feedback response to chronic lipid accumulation and impaired beta-oxidation capacity. ACACB encodes acetyl-CoA carboxylase-β (ACC2), which generates malonyl-CoA, a potent allosteric inhibitor of carnitine palmitoyltransferase 1 (CPT1), the rate-limiting enzyme for mitochondrial long-chain fatty acid uptake and β-oxidation. Elevated ACACB expression may therefore reflect a maladaptive feedback response to chronic lipid accumulation and impaired β-oxidation capacity, whereby higher malonyl-CoA levels act to restrain excessive fatty acid flux into mitochondria under sustained metabolic stress. While this interpretation remains speculative, the convergence of this molecular signature across species and pathological contexts suggests a broader axis of vulnerability in chronic neurodegenerative states marked by PUFA dysregulation and vascular compromise.

Notably, these causal links were empirically demonstrated under controlled, injury-relevant conditions in both *in vivo* and *in vitro* systems. Moreover, our postmortem human CTE brain tissue analysis provides a translationally significant but observational window into chronic disease and underscores a shared vulnerability axis across models and disease. Our findings establish a consistent association between cerebral EPA depletion and vascular gene-expression patterns enriched for endothelial and ECM remodeling pathways. While the present study does not resolve causality, the convergence of lipidomic, transcriptomic, and phenotypic data across *in vivo*, *in vitro*, and human models represents a significant conceptual advance. We propose that PPARα-driven β-oxidation may initially serve as an adaptive response to injury-induced energy demand, but with chronic EPA exposure or impaired vascular repair, this axis may become maladaptive and contribute to progressive neurovascular dysfunction. Future work integrating targeted metabolic flux profiling and receptor-specific modulation will be critical to elucidate the directionality and therapeutic implications of this lipid–vascular axis.

This convergence of experimentally defined mechanisms with disease-associated molecular signatures suggests that maladaptive PUFA handling may be an overlooked contributor to neurovascular compromise in chronic brain injury. Nevertheless, further investigation is warranted to elucidate whether these molecular signatures in CTE reflect initiating pathogenic events or secondary adaptations to cumulative injury. Our findings challenge the prevailing assumption that all omega-3 fatty acids confer uniform benefit across physiological states, instead supporting a paradigm in which dietary PUFA effects are highly context-dependent. We also acknowledge the absence of metabolomic profiling as a limitation; future integration with lipidomic and flux-based approaches will be essential to fully define EPA's metabolic fate and downstream signaling effects *in vivo*. This conceptual shift carries important implications for precision nutritional guidance, therapeutic lipid formulation, and the design of interventional trials, not only for TBI-related neurodegeneration but also for chronic neurological conditions in metabolically vulnerable populations.

Limitations of the study

This study integrates dietary manipulation, neurovascular phenotyping, multiomics, mechanistic endothelial assays, and human postmortem tissue analysis to define an EPA-associated vulnerability following repetitive mild brain injury. Several limitations should be considered when interpreting these findings. First, bulk cortical transcriptomics cannot assign lipid metabolic and vascular gene-expression programs to a single cell type; therefore, future single-cell and spatial profiling will be important for localizing these injury-associated programs within the neurovascular unit. Second, the postmortem CTE analyses provide translationally meaningful alignment with the experimental models but remain observational and cannot establish directionality or causality between omega-3 remodeling and vascular dysfunction. Third, *in silico* target and pathway predictions are hypothesis-generating and require direct experimental validation with receptor-level assays, genetic perturbation, and metabolic flux-based approaches. Fourth, our *in vitro* system models a permissive metabolic state that supports causal testing of endothelial repair phenotypes, but it does not fully capture the multicellular inflammatory, matrix, and hemodynamic features that shape vascular adaptation after brain injury. Finally, our *in vivo* studies were performed in male mice only, which improves internal consistency but limits inference regarding sex dependent differences in omega-3 handling and neurovascular repair after repetitive mild injury. Likewise, the postmortem human arm included male donors only, reflecting tissue availability for this cohort and region, and therefore does not address whether similar lipid metabolic and vascular signatures are present in female CTE.

An additional limitation relates to contextual variables that likely shape omega-3 handling and neurovascular resilience, particularly in human disease. Premorbid factors such as diet and supplementation history, lifestyle and activity profiles, medication exposure, vascular comorbidities, and genetic background are not fully available for the CTE cohort. Peripheral lipid profiling is also not consistently accessible, which limits direct linkage between systemic exposure and brain lipid content. These gaps reinforce a broader, clinically relevant concept: the effects of omega-3 exposure following repetitive head impacts are context-dependent and may differ across individuals based on baseline metabolism and exposure history. This issue is especially relevant to neurology and psychiatry, where cumulative environmental factors often modulate vulnerability and clinical trajectory. Relatedly, while repetitive head impact is a major

risk factor for CTE, it is not deterministically causal, and unmeasured modifiers likely contribute to disease heterogeneity. In this study, we deliberately prioritize brain regions with robust tau pathology to maximize disease signal, but future work could extend these analyses to less affected regions to test whether similar metabolic shifts emerge outside canonical disease territories and to clarify how metabolic remodeling relates to regional vulnerability and progression.

RESOURCE AVAILABILITY

Lead contact

Requests for further information and resources should be directed to and will be fulfilled by the lead contact, Onder Albayram, PhD. (albayram@musc.edu).

Materials availability

This study did not generate new, unique reagents.

Data and code availability

- Data: no standardized dataset was generated in this study. All raw data, experimental and analysis methods, and original images supporting the findings of this study are available upon request from the corresponding author.
- Sequencing data are available at Gene Expression Omnibus, GEO: GSE319252 and GSE319253.
- Code: this study does not report original code.
- Additional information: any additional information required to reanalyze the data reported in this paper is available from the lead contact upon request.

ACKNOWLEDGMENTS

The authors gratefully acknowledge the Hammerbacher family for their generous donation of an imaging system to our laboratory. This work was supported by research grants from the South Carolina Alzheimer's Disease Research Center (ADRC) pilot grant; the COBRE in Neurodevelopment and Its Disorders P20GM148302 research grant; MUSC Specialized Center of Research Excellence (SCORE) U54DA16511 to E.K., B.B., D.B., and O.A.; and the National Cancer Institute (R37CA292807), Oliver S. and Jennie R. Donaldson Charitable Trust, the G. Harold and Leila Y. Mathers Charitable Foundation, the Mark Foundation for Cancer Research (20-028-EDV), the Cold Spring Harbor Laboratory, Northwell Health Affiliation and Swim Across America to S.B. and O.E.; P30AG072978, U01NS086659, and U54NS115266 to A.M. and T.S.; VA Merit Review (BX000347); VA Senior Research Career Scientist award (IK6 BX004471); and NIH RF1 NS083559 and RF1 NS10457 to A.E.

AUTHOR CONTRIBUTIONS

E.K., B.B., S.B., and O.A. designed the research; E.K., B.B., O.E., J.E., R.B., S.J., W.L., Y.A., and M.E. performed the study and analyzed data; A.M., T.S., A.E., S.B., and O.A. provided scientific direction; E.K., B.B., S.B., and O.A. wrote the paper.

DECLARATION OF INTERESTS

The authors declare no competing interests.

STAR★METHODS

Detailed methods are provided in the online version of this paper and include the following:

SUPPLEMENTAL INFORMATION

Supplemental information can be found online at https://doi.org/10.1016/j.celrep.2026.117135.

Received: August 29, 2025
Revised: January 2, 2026
Accepted: February 24, 2026
Published: March 25, 2026

REFERENCES

1. Faul, M., Xu, L., Wald, M.M., and Coronado, V.G. (2010). Traumatic brain injury in the United States: emergency department visits, hospitalizations, and deaths, 2002–2006. http://www.cdc.gov/traumaticbraininjury/tbi_ed.html.
2. Centers for Disease Control and Prevention CDC (2007). Nonfatal traumatic brain injuries from sports and recreation activities — United States, 2001–2005. MMWR (Morb. Mortal. Wkly. Rep.) *56*, 733–737. http://www.cdc.gov/mmwr/preview/mmwrhtml/mm5629a5622.htm.
3. Weinberger, S. (2011). Bombs' hidden impact: the brain war. Nature *477*, 390–393. https://doi.org/10.1038/477390a.
4. Miller, G. (2011). The invisible wounds of war. Healing the brain, healing the mind. Science *333*, 514–517. https://doi.org/10.1126/science.333.6042.514.
5. Marin, J.R., Weaver, M.D., Yealy, D.M., and Mannix, R.C. (2014). Trends in visits for traumatic brain injury to emergency departments in the United States. JAMA *311*, 1917–1919. https://doi.org/10.1001/jama.2014.3979.
6. Abrahamson, E.E., and Ikonomovic, M.D. (2020). Brain injury-induced dysfunction of the blood brain barrier as a risk for dementia. Exp. Neurol. *328*, 113257. https://doi.org/10.1016/j.expneurol.2020.113257.
7. Acosta, C.H., Clemons, G.A., Citadin, C.T., Carr, W.C., Udo, M.S.B., Tesic, V., Sanicola, H.W., Freelin, A.H., Toms, J.B., Jordan, J.D., et al. (2023). PRMT7 can prevent neurovascular uncoupling, blood-brain barrier permeability, and mitochondrial dysfunction in repetitive and mild

traumatic brain injury. Exp. Neurol. *366*, 114445. https://doi.org/10.1016/j.expneurol.2023.114445.

8. Kenney, K., Amyot, F., Haber, M., Pronger, A., Bogoslovsky, T., Moore, C., and Diaz-Arrastia, R. (2016). Cerebral Vascular Injury in Traumatic Brain Injury. Exp. Neurol. *275*, 353–366. https://doi.org/10.1016/j.expneurol.2015.05.019.
9. MacLean, M.A., Muradov, J.H., Greene, R., Van Hameren, G., Clarke, D.B., Dreier, J.P., Okonkwo, D.O., and Friedman, A. (2023). Memantine inhibits cortical spreading depolarization and improves neurovascular function following repetitive traumatic brain injury. Sci. Adv. *9*, eadj2417. https://doi.org/10.1126/sciadv.adj2417.
10. Ramos-Cejudo, J., Wisniewski, T., Marmar, C., Zetterberg, H., Blennow, K., de Leon, M.J., and Fossati, S. (2018). Traumatic Brain Injury and Alzheimer's Disease: The Cerebrovascular Link. EBioMedicine *28*, 21–30. https://doi.org/10.1016/j.ebiom.2018.01.021.
11. Smith, D.H., Johnson, V.E., and Stewart, W. (2013). Chronic neuropathologies of single and repetitive TBI: substrates of dementia? Nat. Rev. Neurol. *9*, 211–221. https://doi.org/10.1038/nrneurol.2013.29.
12. DeKosky, S.T., Blennow, K., Ikonomovic, M.D., and Gandy, S. (2013). Acute and chronic traumatic encephalopathies: pathogenesis and biomarkers. Nat. Rev. Neurol. *9*, 192–200. https://doi.org/10.1038/nrneurol.2013.36.
13. Blennow, K., Hardy, J., and Zetterberg, H. (2012). The neuropathology and neurobiology of traumatic brain injury. Neuron *76*, 886–899. https://doi.org/10.1016/j.neuron.2012.11.021.
14. McKee, A.C., Stern, R.A., Nowinski, C.J., Stein, T.D., Alvarez, V.E., Daneshvar, D.H., Lee, H.S., Wojtowicz, S.M., Hall, G., Baugh, C.M., et al. (2013). The spectrum of disease in chronic traumatic encephalopathy. Brain *136*, 43–64. https://doi.org/10.1093/brain/aws307.
15. Lye, T.C., and Shores, E.A. (2000). Traumatic brain injury as a risk factor for Alzheimer's disease: a review. Neuropsychol. Rev. *10*, 115–129.
16. Nordström, P., Michaëlsson, K., Gustafson, Y., and Nordström, A. (2014). Traumatic brain injury and young onset dementia: a nationwide cohort study. Ann. Neurol. *75*, 374–381.
17. Albayram, O., Angeli, P., Bernstein, E., Baxley, S., Gao, Z., Lu, K.P., and Zhou, X.Z. (2018). Targeting Prion-like Cis Phosphorylated Tau Pathology in Neurodegenerative Diseases. J. Alzheimers Dis. Parkinsonism *8*, 443. https://doi.org/10.4172/2161-0460.1000443.
18. Albayram, O., Herbert, M.K., Kondo, A., Tsai, C.Y., Baxley, S., Lian, X., Hansen, M., Zhou, X.Z., and Lu, K.P. (2016). Function and regulation of tau conformations in the development and treatment of traumatic brain injury and neurodegeneration. Cell Biosci. *6*, 59. https://doi.org/10.1186/s13578-016-0124-4.
19. Albayram, O., Kondo, A., Mannix, R., Smith, C., Tsai, C.Y., Li, C., Herbert, M.K., Qiu, J., Monuteaux, M., Driver, J., et al. (2017). Cis P-tau is induced in clinical and preclinical brain injury and contributes to post-injury sequelae. Nat. Commun. *8*, 1000. https://doi.org/10.1038/s41467-017-01068-4.
20. Kondo, A., Albayram, O., Zhou, X.Z., and Lu, K.P. (2017). Pin1 Knockout Mice: A Model for the Study of Tau Pathology in Alzheimer's Disease. Methods Mol. Biol. *1523*, 415–425. https://doi.org/10.1007/978-1-4939-6598-4_28.
21. Levin, H.S., and Diaz-Arrastia, R.R. (2015). Diagnosis, prognosis, and clinical management of mild traumatic brain injury. Lancet Neurol. *14*, 506–517. https://doi.org/10.1016/S1474-4422(15)00002-2.
22. Albayram, O., Albayram, S., and Mannix, R. (2020). Chronic traumatic encephalopathy-a blueprint for the bridge between neurological and psychiatric disorders. Transl. Psychiatry *10*, 424. https://doi.org/10.1038/s41398-020-01111-x.
23. National Academies of Sciences, Engineering, and Medicine; Health and Medicine Division; Board on Health Care Services; Board on Health Sciences Policy; Committee on Accelerating Progress in Traumatic Brain Injury Research and Care (2022). In Traumatic Brain Injury: A Roadmap for Accelerating Progress, C. Matney, K. Bowman, and D. Berwick, eds. (National Academies Press).
24. Peters, M.E., and Gardner, R.C. (2018). Traumatic brain injury in older adults: do we need a different approach? Concussion *3*, CNC56. https://doi.org/10.2217/cnc-2018-0001.
25. Corrigan, J.D., and Hammond, F.M. (2013). Traumatic brain injury as a chronic health condition. Arch. Phys. Med. Rehabil. *94*, 1199–1201. https://doi.org/10.1016/j.apmr.2013.01.023.
26. Wilson, L., Stewart, W., Dams-O'Connor, K., Diaz-Arrastia, R., Horton, L., Menon, D.K., and Polinder, S. (2017). The chronic and evolving neurological consequences of traumatic brain injury. Lancet Neurol. *16*, 813–825. https://doi.org/10.1016/S1474-4422(17)30279-X.
27. Sweeney, M.D., Kisler, K., Montagne, A., Toga, A.W., and Zlokovic, B.V. (2018). The role of brain vasculature in neurodegenerative disorders. Nat. Neurosci. *21*, 1318–1331. https://doi.org/10.1038/s41593-018-0234-x.
28. Hay, J.R., Johnson, V.E., Young, A.M.H., Smith, D.H., and Stewart, W. (2015). Blood-Brain Barrier Disruption Is an Early Event That May Persist for Many Years After Traumatic Brain Injury in Humans. J. Neuropathol. Exp. Neurol. *74*, 1147–1157. https://doi.org/10.1097/NEN.0000000000000261.
29. Sandsmark, D.K., Bashir, A., Wellington, C.L., and Diaz-Arrastia, R. (2019). Cerebral Microvascular Injury: A Potentially Treatable Endophenotype of Traumatic Brain Injury-Induced Neurodegeneration. Neuron *103*, 367–379. https://doi.org/10.1016/j.neuron.2019.06.002.
30. Crider, T., Eng, D., Sarkar, P.R., Cordero, J., Krusz, J.C., and Sarkar, S.N. (2018). Microvascular and large vein abnormalities in young patients after mild head trauma and associated fatigue: A brain SPECT evaluation and posture dependence modeling. Clin. Neurol. Neurosurg. *170*, 159–164. https://doi.org/10.1016/j.clineuro.2018.05.019.
31. Weil, Z.M., Karelina, K., Whitehead, B., Velazquez-Cruz, R., Oliverio, R., Pinti, M., Nwafor, D.C., Nicholson, S., Fitzgerald, J.A., Hollander, J., et al. (2021). Mild traumatic brain injury increases vulnerability to cerebral ischemia in mice. Exp. Neurol. *342*, 113765. https://doi.org/10.1016/j.expneurol.2021.113765.
32. Wendel, K.M., Lee, J.B., Affeldt, B.M., Hamer, M., Harahap-Carrillo, I.S., Pardo, A.C., and Obenaus, A. (2019). Corpus Callosum Vasculature Predicts White Matter Microstructure Abnormalities after Pediatric Mild Traumatic Brain Injury. J. Neurotrauma *36*, 152–164. https://doi.org/10.1089/neu.2018.5670.
33. Wu, Y., Wu, H., Zeng, J., Pluimer, B., Dong, S., Xie, X., Guo, X., Ge, T., Liang, X., Feng, S., et al. (2021). Mild traumatic brain injury induces microvascular injury and accelerates Alzheimer-like pathogenesis in mice. Acta Neuropathol. Commun. *9*, 74. https://doi.org/10.1186/s40478-021-01178-7.
34. Zhao, Z.A., Yan, L., Wen, J., Satyanarayanan, S.K., Yu, F., Lu, J., Liu, Y.U., and Su, H. (2023). Cellular and molecular mechanisms in vascular repair after traumatic brain injury: a narrative review. Burns Trauma *11*, tkad033. https://doi.org/10.1093/burnst/tkad033.
35. Risau, W. (1997). Mechanisms of angiogenesis. Nature *386*, 671–674. https://doi.org/10.1038/386671a0.
36. Hynes, R.O. (2009). The extracellular matrix: not just pretty fibrils. Science *326*, 1216–1219. https://doi.org/10.1126/science.1176009.
37. Salehi, A., Zhang, J.H., and Obenaus, A. (2017). Response of the cerebral vasculature following traumatic brain injury. J. Cereb. Blood Flow Metab. *37*, 2320–2339. https://doi.org/10.1177/0271678X17701460.
38. Bazinet, R.P., and Layé, S. (2014). Polyunsaturated fatty acids and their metabolites in brain function and disease. Nat. Rev. Neurosci. *15*, 771–785. https://doi.org/10.1038/nrn3820.
39. Baumgartner, J., Smuts, C.M., Malan, L., Arnold, M., Yee, B.K., Bianco, L.E., Boekschoten, M.V., Müller, M., Langhans, W., Hurrell, R.F., et al. (2012). In male rats with concurrent iron and (n-3) fatty acid deficiency, provision of either iron or (n-3) fatty acids alone alters monoamine

metabolism and exacerbates the cognitive deficits associated with combined deficiency. J. Nutr. *142*, 1472–1478. https://doi.org/10.3945/jn.111.156299.

40. Liu, J.H., Wang, Q., You, Q.L., Li, Z.L., Hu, N.Y., Wang, Y., Jin, Z.L., Li, S.J., Li, X.W., Yang, J.M., et al. (2020). Acute EPA-induced learning and memory impairment in mice is prevented by DHA. Nat. Commun. *11*, 5465. https://doi.org/10.1038/s41467-020-19255-1.

41. Pifferi, F., Cunnane, S.C., and Guesnet, P. (2020). Evidence of the Role of Omega-3 Polyunsaturated Fatty Acids in Brain Glucose Metabolism. Nutrients *12*, 1382. https://doi.org/10.3390/nu12051382.

42. van Elst, K., Brouwers, J.F., Merkens, J.E., Broekhoven, M.H., Birtoli, B., Helms, J.B., and Kas, M.J.H. (2019). Chronic dietary changes in n-6/n-3 polyunsaturated fatty acid ratios cause developmental delay and reduce social interest in mice. Eur. Neuropsychopharmacol. *29*, 16–31. https://doi.org/10.1016/j.euroneuro.2018.11.1106.

43. Yang, D.Y., Pan, H.C., Yen, Y.J., Wang, C.C., Chuang, Y.H., Chen, S.Y., Lin, S.Y., Liao, S.L., Raung, S.L., Wu, C.W., et al. (2007). Detrimental effects of post-treatment with fatty acids on brain injury in ischemic rats. Neurotoxicology *28*, 1220–1229. https://doi.org/10.1016/j.neuro.2007.08.003.

44. Connor, K.M., SanGiovanni, J.P., Lofqvist, C., Aderman, C.M., Chen, J., Higuchi, A., Hong, S., Pravda, E.A., Majchrzak, S., Carper, D., et al. (2007). Increased dietary intake of omega-3-polyunsaturated fatty acids reduces pathological retinal angiogenesis. Nat. Med. *13*, 868–873. https://doi.org/10.1038/nm1591.

45. Kermorvant-Duchemin, E., Sennlaub, F., Sirinyan, M., Brault, S., Andelfinger, G., Kooli, A., Germain, S., Ong, H., d'Orleans-Juste, P., Gobeil, F., Jr., et al. (2005). Trans-arachidonic acids generated during nitrative stress induce a thrombospondin-1-dependent microvascular degeneration. Nat. Med. *11*, 1339–1345. https://doi.org/10.1038/nm1336.

46. Sapieha, P., Stahl, A., Chen, J., Seaward, M.R., Willett, K.L., Krah, N.M., Dennison, R.J., Connor, K.M., Aderman, C.M., Liclican, E., et al. (2011). 5-Lipoxygenase metabolite 4-HDHA is a mediator of the antiangiogenic effect of omega-3 polyunsaturated fatty acids. Sci. Transl. Med. *3*, 69ra12. https://doi.org/10.1126/scitranslmed.3001571.

47. Karakaya, E., Oleinik, N., Edwards, J., Tomberlin, J., Barker, R.B., Berber, B., Ericsson, M., Alsudani, H., Ergul, A., Beyaz, S., et al. (2024). p17/C18-ceramide-mediated mitophagy is an endogenous neuroprotective response in preclinical and clinical brain injury. PNAS Nexus *3*, pgae018. https://doi.org/10.1093/pnasnexus/pgae018.

48. De Bock, K., Georgiadou, M., Schoors, S., Kuchnio, A., Wong, B.W., Cantelmo, A.R., Quaegebeur, A., Ghesquière, B., Cauwenberghs, S., Eelen, G., et al. (2013). Role of PFKFB3-driven glycolysis in vessel sprouting. Cell *154*, 651–663. https://doi.org/10.1016/j.cell.2013.06.037.

49. Liu, B., and Dai, Z. (2022). Fatty Acid Metabolism in Endothelial Cell. Genes *13*, 2301. https://doi.org/10.3390/genes13122301.

50. Schönfeld, P., and Reiser, G. (2013). Why does brain metabolism not favor burning of fatty acids to provide energy? Reflections on disadvantages of the use of free fatty acids as fuel for brain. J. Cereb. Blood Flow Metab. *33*, 1493–1499. https://doi.org/10.1038/jcbfm.2013.128.

51. Fernandez, R.F., Kim, S.Q., Zhao, Y., Foguth, R.M., Weera, M.M., Counihan, J.L., Nomura, D.K., Chester, J.A., Cannon, J.R., and Ellis, J.M. (2018). Acyl-CoA synthetase 6 enriches the neuroprotective omega-3 fatty acid DHA in the brain. Proc. Natl. Acad. Sci. USA *115*, 12525–12530. https://doi.org/10.1073/pnas.1807958115.

52. Morant-Ferrando, B., Jimenez-Blasco, D., Alonso-Batan, P., Agulla, J., Lapresa, R., Garcia-Rodriguez, D., Yunta-Sanchez, S., Lopez-Fabuel, I., Fernandez, E., Carmeliet, P., et al. (2023). Fatty acid oxidation organizes mitochondrial supercomplexes to sustain astrocytic ROS and cognition. Nat. Metab. *5*, 1290–1302. https://doi.org/10.1038/s42255-023-00835-6.

53. Arterburn, L.M., Hall, E.B., and Oken, H. (2006). Distribution, interconversion, and dose response of n-3 fatty acids in humans. Am. J. Clin. Nutr. *83*, 1467S–1476S. https://doi.org/10.1093/ajcn/83.6.1467S.

54. Domenichiello, A.F., Chen, C.T., Trepanier, M.O., Stavro, P.M., and Bazinet, R.P. (2014). Whole body synthesis rates of DHA from alpha-linolenic acid are greater than brain DHA accretion and uptake rates in adult rats. J. Lipid Res. *55*, 62–74. https://doi.org/10.1194/jlr.M042275.

55. Domenichiello, A.F., Kitson, A.P., and Bazinet, R.P. (2015). Is docosahexaenoic acid synthesis from alpha-linolenic acid sufficient to supply the adult brain? Prog. Lipid Res. *59*, 54–66. https://doi.org/10.1016/j.plipres.2015.04.002.

56. Lefkowitz, W., Lim, S.Y., Lin, Y., and Salem, N., Jr. (2005). Where does the developing brain obtain its docosahexaenoic acid? Relative contributions of dietary alpha-linolenic acid, docosahexaenoic acid, and body stores in the developing rat. Pediatr. Res. *57*, 157–165. https://doi.org/10.1203/01.PDR.0000147572.57627.AE.

57. Hayden, M.R. (2024). Cerebral Microbleeds Associate with Brain Endothelial Cell Activation-Dysfunction and Blood-Brain Barrier Dysfunction/Disruption with Increased Risk of Hemorrhagic and Ischemic Stroke. Biomedicines *12*, 1463. https://doi.org/10.3390/biomedicines12071463.

58. Li, G.S., Wang, X.X., Tan, R.B., Wang, K.H., Hu, X.S., and Hu, Y. (2022). Ultrastructural destruction of neurovascular unit in experimental cervical spondylotic myelopathy. Front. Neurosci. *16*, 1031180. https://doi.org/10.3389/fnins.2022.1031180.

59. Bilkei-Gorzo, A., Albayram, O., Draffehn, A., Michel, K., Piyanova, A., Oppenheimer, H., Dvir-Ginzberg, M., Rácz, I., Ulas, T., Imbeault, S., et al. (2017). A chronic low dose of Delta(9)-tetrahydrocannabinol (THC) restores cognitive function in old mice. Nat. Med. *23*, 782–787. https://doi.org/10.1038/nm.4311.

60. Bonneh-Barkay, D., and Wiley, C.A. (2009). Brain extracellular matrix in neurodegeneration. Brain Pathol. *19*, 573–585. https://doi.org/10.1111/j.1750-3639.2008.00195.x.

61. Liebner, S., Czupalla, C.J., and Wolburg, H. (2011). Current concepts of blood-brain barrier development. Int. J. Dev. Biol. *55*, 467–476. https://doi.org/10.1387/ijdb.103224sl.

62. Soles, A., Selimovic, A., Sbrocco, K., Ghannoum, F., Hamel, K., Moncada, E.L., Gilliat, S., and Cvetanovic, M. (2023). Extracellular Matrix Regulation in Physiology and in Brain Disease. Int. J. Mol. Sci. *24*, 7049. https://doi.org/10.3390/ijms24087049.

63. Gatseva, A., Sin, Y.Y., Brezzo, G., and Van Agtmael, T. (2019). Basement membrane collagens and disease mechanisms. Essays Biochem. *63*, 297–312. https://doi.org/10.1042/EBC20180071.

64. Thomsen, M.S., Routhe, L.J., and Moos, T. (2017). The vascular basement membrane in the healthy and pathological brain. J. Cereb. Blood Flow Metab. *37*, 3300–3317. https://doi.org/10.1177/0271678X17722436.

65. Volonghi, I., Pezzini, A., Del Zotto, E., Giossi, A., Costa, P., Ferrari, D., and Padovani, A. (2010). Role of COL4A1 in basement-membrane integrity and cerebral small-vessel disease. The COL4A1 stroke syndrome. Curr. Med. Chem. *17*, 1317–1324. https://doi.org/10.2174/092986710790936293.

66. Chmelova, M., Androvic, P., Kirdajova, D., Tureckova, J., Kriska, J., Valihrach, L., Anderova, M., and Vargova, L. (2023). A view of the genetic and proteomic profile of extracellular matrix molecules in aging and stroke. Front. Cell. Neurosci. *17*, 1296455. https://doi.org/10.3389/fncel.2023.1296455.

67. Gottschall, P.E., and Howell, M.D. (2015). ADAMTS expression and function in central nervous system injury and disorders. Matrix Biol. *44–46*, 70–76. https://doi.org/10.1016/j.matbio.2015.01.014.

68. Mohamedi, Y., Fontanil, T., Cobo, T., Cal, S., and Obaya, A.J. (2020). New Insights into ADAMTS Metalloproteases in the Central Nervous System. Biomolecules *10*, 403. https://doi.org/10.3390/biom10030403.

69. Custers, Emma, E.M., Emma, E.M., Kiliaan, and Amanda, J. (2022). Dietary lipids from body to brain. Prog. Lipid Res. *85*, 101144. https://doi.org/10.1016/j.plipres.2021.101144.

70. Hussain, Y., Dar, M.I., and Pan, X. (2024). Circadian Influences on Brain Lipid Metabolism and Neurodegenerative Diseases. Metabolites *14*, 723. https://doi.org/10.3390/metabo14120723.

71. Murru, E., Carta, G., Manca, C., Sogos, V., Pistis, M., Melis, M., and Banni, S. (2020). Conjugated Linoleic Acid and Brain Metabolism: A Possible Anti-Neuroinflammatory Role Mediated by PPARalpha Activation. Front. Pharmacol. *11*, 587140. https://doi.org/10.3389/fphar.2020.587140.

72. Pifferi, F., Laurent, B., and Plourde, M. (2021). Lipid Transport and Metabolism at the Blood-Brain Interface: Implications in Health and Disease. Front. Physiol. *12*, 645646. https://doi.org/10.3389/fphys.2021.645646.

73. Elmasri, H., Ghelfi, E., Yu, C.W., Traphagen, S., Cernadas, M., Cao, H., Shi, G.P., Plutzky, J., Sahin, M., Hotamisligil, G., et al. (2012). Endothelial cell-fatty acid binding protein 4 promotes angiogenesis: role of stem cell factor/c-kit pathway. Angiogenesis *15*, 457–468. https://doi.org/10.1007/s10456-012-9274-0.

74. Hu, C., Tao, L., Cao, X., and Chen, L. (2020). The solute carrier transporters and the brain: Physiological and pharmacological implications. Asian J. Pharm. Sci. *15*, 131–144. https://doi.org/10.1016/j.ajps.2019.09.002.

75. Lin, L., Yee, S.W., Kim, R.B., and Giacomini, K.M. (2015). SLC transporters as therapeutic targets: emerging opportunities. Nat. Rev. Drug Discov. *14*, 543–560. https://doi.org/10.1038/nrd4626.

76. Simpson, I.A., Carruthers, A., and Vannucci, S.J. (2007). Supply and demand in cerebral energy metabolism: the role of nutrient transporters. J. Cereb. Blood Flow Metab. *27*, 1766–1791. https://doi.org/10.1038/sj.jcbfm.9600521.

77. Greenberg, D.A., and Jin, K. (2005). From angiogenesis to neuropathology. Nature *438*, 954–959. https://doi.org/10.1038/nature04481.

78. Dagher, Z., Ruderman, N., Tornheim, K., and Ido, Y. (2001). Acute regulation of fatty acid oxidation and amp-activated protein kinase in human umbilical vein endothelial cells. Circ. Res. *88*, 1276–1282. https://doi.org/10.1161/hh1201.092998.

79. Mayurasakorn, K., Niatsetskaya, Z.V., Sosunov, S.A., Williams, J.J., Zirpoli, H., Vlasakov, I., Deckelbaum, R.J., and Ten, V.S. (2016). DHA but Not EPA Emulsions Preserve Neurological and Mitochondrial Function after Brain Hypoxia-Ischemia in Neonatal Mice. PLoS One *11*, e0160870. https://doi.org/10.1371/journal.pone.0160870.

80. Bailes, J.E., Abusuwwa, R., Arshad, M., Chowdhry, S.A., Schleicher, D., Hempeck, N., Gandhi, Y.N., Jaffa, Z., Bokhari, F., Karahalios, D., et al. (2020). Omega-3 fatty acid supplementation in severe brain trauma: case for a large multicenter trial. J. Neurosurg. *133*, 598–602. https://doi.org/10.3171/2020.3.JNS20183.

81. Bradbury, J. (2011). Docosahexaenoic acid (DHA): an ancient nutrient for the modern human brain. Nutrients *3*, 529–554. https://doi.org/10.3390/nu3050529.

82. Dyall, S.C. (2015). Long-chain omega-3 fatty acids and the brain: a review of the independent and shared effects of EPA, DPA and DHA. Front. Aging Neurosci. *7*, 52. https://doi.org/10.3389/fnagi.2015.00052.

83. McNamara, R.K. (2013). Deciphering the role of docosahexaenoic acid in brain maturation and pathology with magnetic resonance imaging. Prostaglandins Leukot. Essent. Fatty Acids *88*, 33–42. https://doi.org/10.1016/j.plefa.2012.03.011.

84. Jullienne, A., Roberts, J.M., Pop, V., Paul Murphy, M., Head, E., Bix, G.J., and Badaut, J. (2014). Juvenile traumatic brain injury induces long-term perivascular matrix changes alongside amyloid-beta accumulation. J. Cereb. Blood Flow Metab. *34*, 1637–1645. https://doi.org/10.1038/jcbfm.2014.124.

85. Iadecola, C. (2017). The Neurovascular Unit Coming of Age: A Journey through Neurovascular Coupling in Health and Disease. Neuron *96*, 17–42. https://doi.org/10.1016/j.neuron.2017.07.030.

86. Quinn, D.K., Upston, J., Jones, T., Brandt, E., Story-Remer, J., Fratzke, V., Wilson, J.K., Rieger, R., Hunter, M.A., Gill, D., et al. (2020). Cerebral Perfusion Effects of Cognitive Training and Transcranial Direct Current Stimulation in Mild-Moderate TBI. Front. Neurol. *11*, 545174. https://doi.org/10.3389/fneur.2020.545174.

87. Sheng, L., Zheng, X., Ding, Z., Liu, J., and Song, W. (2025). Neurovascular coupling dysfunction in encephalopathy: pathophysiological advances and clinical implications. Front. Neurol. *16*, 1522485. https://doi.org/10.3389/fneur.2025.1522485.

88. Mathew, S.A., and Bhonde, R.R. (2018). Omega-3 polyunsaturated fatty acids promote angiogenesis in placenta derived mesenchymal stromal cells. Pharmacol. Res. *132*, 90–98. https://doi.org/10.1016/j.phrs.2018.04.002.

89. Peng, J., Zhou, Y., Hong, Z., Wu, Y., Cai, A., Xia, M., Deng, Z., Yang, Y., Song, T., Xiong, J., et al. (2019). Maternal eicosapentaenoic acid feeding promotes placental angiogenesis through a Sirtuin-1 independent inflammatory pathway. Biochim. Biophys. Acta. Mol. Cell Biol. Lipids *1864*, 147–157. https://doi.org/10.1016/j.bbalip.2018.11.003.

90. Kondo, A., Shahpasand, K., Mannix, R., Qiu, J., Moncaster, J., Chen, C.H., Yao, Y., Lin, Y.M., Driver, J.A., Sun, Y., et al. (2015). Antibody against early driver of neurodegeneration cis P-tau blocks brain injury and tauopathy. Nature *523*, 431–436. https://doi.org/10.1038/nature14658.

91. Mannix, R., Berkner, J., Mei, Z., Alcon, S., Hashim, J., Robinson, S., Jantzie, L., Meehan, W.P., 3rd, and Qiu, J. (2017). Adolescent Mice Demonstrate a Distinct Pattern of Injury after Repetitive Mild Traumatic Brain Injury. J. Neurotrauma *34*, 495–504. https://doi.org/10.1089/neu.2016.4457.

92. Qiu, C., Albayram, O., Kondo, A., Wang, B., Kim, N., Arai, K., Tsai, C.Y., Bassal, M.A., Herbert, M.K., Washida, K., et al. (2021). Cis P-tau underlies vascular contribution to cognitive impairment and dementia and can be effectively targeted by immunotherapy in mice. Sci. Transl. Med. *13*, eaaz7615. https://doi.org/10.1126/scitranslmed.aaz7615.

93. Robinson, S., Berglass, J.B., Denson, J.L., Berkner, J., Anstine, C.V., Winer, J.L., Maxwell, J.R., Qiu, J., Yang, Y., Sillerud, L.O., et al. (2017). Microstructural and microglial changes after repetitive mild traumatic brain injury in mice. J. Neurosci. Res. *95*, 1025–1035. https://doi.org/10.1002/jnr.23848.

94. Bielawski, J., Pierce, J.S., Snider, J., Rembiesa, B., Szulc, Z.M., and Bielawska, A. (2009). Comprehensive quantitative analysis of bioactive sphingolipids by high-performance liquid chromatography-tandem mass spectrometry. Methods Mol. Biol. *579*, 443–467. https://doi.org/10.1007/978-1-60761-322-0_22.

95. Bielawski, J., Pierce, J.S., Snider, J., Rembiesa, B., Szulc, Z.M., and Bielawska, A. (2010). Sphingolipid analysis by high performance liquid chromatography-tandem mass spectrometry (HPLC-MS/MS). Adv. Exp. Med. Biol. *688*, 46–59. https://doi.org/10.1007/978-1-4419-6741-1_3.

96. Bielawski, J., Szulc, Z.M., Hannun, Y.A., and Bielawska, A. (2006). Simultaneous quantitative analysis of bioactive sphingolipids by high-performance liquid chromatography-tandem mass spectrometry. Methods *39*, 82–91. https://doi.org/10.1016/j.ymeth.2006.05.004.

STAR★METHODS

KEY RESOURCES TABLE

REAGENT or RESOURCE	SOURCE	IDENTIFIER
Antibodies		
anti–phospho-tau (Ser202/Thr205)	Thermo Fisher Scientific	Cat # MN1020 RRID:AB_223647
FITC-conjugated Lycopersicon esculentum lectin (LEL 488)	Vector Laboratories	Cat #DL1174 RRID:AB_2336404
anti–collagen type VI alpha 6 (Col6a6)	Novus Biologicals	Cat # NBP2-14546 RRID:AB_3261932
anti-agrin	Novus Biologicals	Cat # NBP1-90209 RRID:AB_11029656
anti–collagen type IV alpha 1 (Col4a1)	Invitrogen	Cat # MA5-47009 RRID:AB_2938081
Calcein AM Viability Dye	Invitrogen	Cat # 65-0853-39 RRID:NA
anti–VE-cadherin	Cell Signaling Tech.	Cat # 93467 RRID:AB_3683680
anti–claudin-5	Invitrogen	Cat # 35-2500 RRID:AB_87321
anti–peroxisome proliferator-activated receptor alpha (PPARα/NR1C1)	Novus Biologicals	Cat # NB600-636 NB600-636; RRID: AB_3195588
anti–matrix metalloproteinase 9 (MMP9)	Invitrogen	Cat # MA5-15886 RRID:AB_11157246
anti–β-actin-peroxidase conjugate	Millipore Sigma	Cat # A3854 RRID:AB_262011
HRP–conjugated secondary antibodies	Bio-Rad	Cat # 1706515 and 1706516 RRID:AB_11125142 or AB_11125547
Biological samples		
Human postmortem brain tissue (superior frontal cortex)	VA BU CLF Brain Bank, Boston University Alzheimer's Disease Center CTE Program	D239
Chemicals, peptides, and recombinant proteins		
Blotting grade blocker NON-FAT DRY MILK	Bio-Rad	Cat # 170-6404
TBS with Tween™ (TBST), 20X, 5L	Thermo Fisher	Cat #J77500.K8
4–12% Bis-Tris polyacrylamide gels	Thermo Fisher	Cat # WG1402BOX
Bovine Serum Albumin (BSA), Fraction V, heat shock treated	Thermo Fisher	Cat # BP1600-100
Immobilon Western Chemiluminescent HRP Substrate	Millipore Sigma	Cat # WBKLS0500
Hydrogen Peroxide	Fisher Chemical	Cat #H325-500
Tween 20	Thermo Fisher	Cat #J20605-AP
PBS (Phosphate Buffer Saline)	Corning	Cat# 21-040-CM
Gelatin	Sigma-Aldrich	Cat# G2500-500G
endothelial cell growth medium	VEC Technologies	Cat# MCDB-131
Medium 199	Fisher Scientific	MT10060CV
penicillin-streptomycin	Thermo Fisher	Cat # 15140122
Fetal bovine serum (FBS)	ATCC	Cat # 30-2020
AICAR (5-Aminoimidazole-4-carboxamide ribonucleotide)	Sigma-Aldrich	Cat # A9978-5mg
L-carnitine	Sigma-Aldrich	Cat# S7957292
Docosahexaenoic acid (DHA)	Sigma-Aldrich	Cat #D2534-100mg

(*Continued on next page*)

Continued

REAGENT or RESOURCE	SOURCE	IDENTIFIER
eicosapentaenoic acid (EPA)	Cayman	Cat # 901110
fatty acid–free BSA	Fisher Bioreagents	Cat # BP9704-100
NaCl	Sigma-Aldrich	Cat #S9888
Growth factor–reduced Matrigel	Corning	Cat # 354230
Calcein-AM	Thermo Scientific	Cat # 65-0853-39
4-MTT (3-(4,5-Dimethylthiazol-2-yl)-2,5-Diphenyltetrazolium Bromide)- M6494 1 g	Thermo Scientific	Cat #M6494
RNeasy Mini Kit	Qiagen	Cat # 74104
High-Capacity cDNA Reverse Transcription Kit	Applied Biosystems	Cat # 4368814
TaqMan Gene Expression Assays	Applied Biosystems	Cat # 4331182
LightCycler 480 SYBR Green I Master Mix	Roche	Cat # 04707516001
Forane (Isoflurane), 100mL	Isospire	N/A
Ketamine HCL INJ 100 MG/ML 5 mL VI	NDC	Cat # 0143-9509-01
Xylazine Injection 100mg/ml, 50 mL	Dechra	Cat # 07-893-8424
Paraformaldehyde 4% Glutaraldehyde 1% In 0.1M Phosphate Buffer pH7.0	Electron Microscopy Sciences	Cat # 15949
Sodium Citrate Buffer (pH = 6)	Thermo Scientific	Cat #J61815.AK
Tri-Sodium Hydrate (MW = 294.1g)	Thermo Scientific	Cat # AC447292500
Distilled Water	Thermo Scientific	Cat # 15230204
Deposited Data		
Raw and analyzed Bulk-RNA Seq data for Mouse	This Paper	GSE319252
Raw and analyzed Bulk-RNA Seq data for Human	This Paper	GSE319253
Experimental models: Cell lines		
Human brain microvascular endothelial cells (HBEC 5i	ATCC	Cat# CRL 3245
Experimental models: Organisms/strains		
Mouse: C57BL/6J	The Jackson Laboratory	Stock No. 000664
Software and algorithms		
Noldus EthoVision XT software	Ethovision	N/A
Amersham Imager 680 system	GE Healthcare	N/A
QUANTL software	GE Healthcare	N/A
Volocity 6.3 software	PerkinElmer	N/A
Fiji/ImageJ Coloc 2	Fiji/ImageJ	N/A
Imaris (Bitplane)	Oxford Instruments	N/A
DESeq2 package	R (v4.2.2)	N/A
ClusterProfiler	R (v4.2.2)	N/A
GraphPad Prism	GraphPad Software	N/A
ECIS software	Applied BioPhysics (ECIS)	N/A

EXPERIMENTAL MODEL AND STUDY PARTICIPANT DETAILS

Animals

Male C57BL/6J wild-type mice (Jackson Laboratory; stock 000664) were used at 2 months of age (young adult). Mice were group housed (n = 4 per cage) in individually ventilated cages containing corncob bedding with *ad libitum* access to standard chow and filtered water. The vivarium was maintained at 22 ± 2°C and 50 ± 10 percent relative humidity under a 12 h light-dark cycle (lights on at 07:00). Animals were assigned to experimental groups based on injury and diet condition as described in the Methods. All procedures were approved by the Institutional Animal Care and Use Committee and conducted in accordance with NIH standards and the Guide for the Care and Use of Laboratory Animals.

Sex as a biological variable (animals)

Only male mice were used. This design reduces variability from estrous cycle-associated hormonal fluctuations but limits the generalizability of findings to females, which is acknowledged as a study limitation.

Human brain specimens

Fresh frozen human brain tissue samples from the superior frontal cortex were obtained from the VA BU CLF Brain Bank at the Boston University Alzheimer's Disease Center CTE Program. The cohort included $n = 6$ neuropathologically confirmed CTE cases and $n = 6$ neurologically healthy controls. Samples were allocated to experimental groups based on neuropathological diagnosis (CTE versus control), with controls selected to be age-matched to the CTE cases. All samples included in the current study were from male donors, reflecting the limited availability of female CTE specimens in the repository for the specified region and case criteria. Available demographic variables included age, sex, weight, and height (Figure S10). Race, ethnicity, ancestry, and nutritional or metabolic intake histories were not available from repository records. All brain donations were obtained with written informed consent from the next of kin. Institutional Review Board approvals for tissue acquisition and use were obtained through the Boston University Alzheimer's Disease Center, the Bedford VA Hospital, and the Boston University School of Medicine. Neuropathological evaluations were performed under IRB-approved protocols.

Sex as a biological variable (human tissue)

Only male postmortem specimens were available for inclusion in this analysis. Accordingly, sex associated differences could not be assessed in the human tissue arm, and the findings should not be generalized to female CTE without additional studies.

Cell lines

Human brain microvascular endothelial cells (HBEC 5i; ATCC CRL 3245), derived from male donor brain microvessels and immortalized with SV40 large T antigen, were cultured in gelatin coated flasks. Cells were maintained in a 1 to 1 mixture of endothelial cell growth medium (VEC Technologies) and Medium 199 (Corning) supplemented with 5 percent fetal bovine serum and 1 percent penicillin streptomycin. Cultures were maintained at 37°C in a humidified 5 percent CO2 atmosphere and passaged at 80 to 90 percent confluence. All experiments were performed using cells within 10 passages from thawing.

Cell line authentication

The HBEC 5i cell line was obtained directly from ATCC. Cell line identity was verified by supplier documentation and expected endothelial morphology. Short tandem repeat profiling was not performed in-house.

Mycoplasma testing

Cultures were routinely screened for mycoplasma contamination prior to experimentation and were negative.

METHOD DETAILS

Cyclic high-fat diet administration

Mice were randomly assigned to receive either a cyclic high-fat diet (HFD) enriched with fish oil (FO)–derived eicosapentaenoic acid (EPA, 20:5*n*-3) and docosahexaenoic acid (DHA, 22:6*n*-3), or a continuous purified control diet. Upon arrival, all animals were acclimated for 48 h on a standardized purified diet (TD.97184; Envigo, Madison, WI, USA). The cyclic HFD group was maintained on a 3-day repeating schedule consisting of two consecutive days on the control diet followed by one day on a 45% HFD enriched with long-chain omega-3 polyunsaturated fatty acids (PUFAs; TD.180549; Envigo) (Figure S11). This intermittent feeding paradigm was designed to emulate human dietary variability and avoid metabolic distortions associated with continuous *ad libitum* high-fat feeding. Control animals remained on the purified diet throughout the study. Diets were exchanged at consistent time intervals, and the remaining food was weighed at each switch to estimate daily caloric intake per cage (kcal/day). The FO–supplemented HFD delivered 82.7 g/kg total PUFAs, including 26.3 g/kg EPA and 20.5 g/kg DHA, both absent from the control diet, which instead contained 42.7 g/kg PUFAs primarily composed of linoleic acid (18:2*n*-6) and α-linolenic acid (18:3*n*-3). The FO-supplemented HFD exhibited a markedly reduced *n*-6:*n*-3 ratio of 0.4, in contrast to 6.6 in the control diet, reflecting a profound shift in lipidomic balance toward omega-3 fatty acids. In addition to EPA and DHA, the FO-supplemented high-fat diet included a broader complement of saturated and monounsaturated fatty acids characteristic of FO–based formulations, such as myristic acid (14:0), palmitic acid (16:0), palmitoleic acid (16:1), and oleic acid (18:1). The purified control diet, by contrast, was primarily enriched in linoleic acid (18:2*n*-6) and α-linolenic acid (18:3*n*-3). These compositional differences reflect the natural lipid profiles of the respective diets and are fully detailed in Figure S11.

Notably, both diets were isocaloric and matched for protein, amino acid, vitamin, and mineral content to eliminate non-lipid nutritional confounds. The dietary intervention commenced one month before repetitive less-than-mild traumatic brain injury (rlmTBI) induction and was sustained for six months after the injury. Metabolic health was monitored weekly through longitudinal body weight measurements. Fasting blood glucose was assessed via tail nick using a calibrated glucometer after a 6-h morning fast. Gonadal fat pads were excised and weighed at the experimental endpoint to quantify adiposity.

Repetitive less-than-mild traumatic brain injury (rlmTBI) model

Mice were randomly assigned to either a cyclic FO–supplemented HFD or a continuous purified control diet for one month before traumatic brain injury (TBI) induction. Following dietary preconditioning, mice were further randomized to receive either

repetitive less-than-mild TBI (rlmTBI) or sham procedures, as previously described.[47] To induce rlmTBI, mice were anesthetized using 4% isoflurane delivered in a 70:30 air:oxygen mixture for exactly 5 min. Anesthetized animals were placed prone on a compliant surface (Kimwipe, Kimberly-Clark, Irving, TX, USA), with the dorsal skull aligned beneath a vertically mounted guide tube. A 54-gram tungsten alloy bolt was released from a height of 24 inches, striking the dorsal cranium with a flat 5 mm-diameter impact tip. The resulting cranial displacement through the Kimwipe produced a non-penetrating, closed-head rotational insult of sub-concussive severity. Each animal in the rlmTBI group received seven impacts across nine days, delivered once daily for five consecutive days, followed by two days without injury, and then two additional daily impacts to complete the seven-impact series.[19,90–93] Sham animals underwent identical anesthesia and handling on the same schedule without impact. Immediately after each impact or sham exposure, animals were assessed for recovery of the righting reflex as a measure of acute neurologic suppression. Righting reflex latency was defined as the time from cessation of anesthesia to spontaneous righting after the animal was placed supine in the recovery cage. For figure display, righting latencies were summarized as block-averaged values across impacts 1–3, 3–5, and 5–7 to reduce trial-level variability and provide a clear representation of acute severity across the impact series. Animals were monitored continuously until spontaneous mobility was restored, after which they were returned to their home cage. No skull fractures, seizures, or overt motor impairment were observed, and all animals survived the full protocol. All procedures were approved by the IACUC and were conducted in accordance with the NIH Guide for the Care and Use of Laboratory Animals.

Behavioral testing

All behavioral assessments were conducted between 10:00 and 15:00 during the lights-on phase at either the Animal Research Facility or the Veterans Affairs Small Animal Behavioral and Physiological Assessment Core. Experimenters were blinded to group allocation throughout the testing procedures. Prior to each test, mice were habituated to the procedure room for 30 min.

Ledge assay

Sensorimotor coordination and balance were evaluated using a ledge-walking assay, as previously established. Mice were individually placed on the narrow ledge of a standard laboratory cage (35 cm height $\times$ 0.8 cm width) and observed for 20 s per trial. Each animal underwent three trials, and behavior was scored in a double-blind manner on a 0–3 scale: 0 = normal ambulation without foot slips; 1 = a single foot fault during traversal; 2 = refusal to walk or immediate dismount; and 3 = fall from the ledge or avoidance of engagement. The mean score across the three trials was used for subsequent analysis.

Morris water maze

The Morris Water Maze (MWM) assessed spatial learning and memory. The apparatus consisted of a circular white pool (83 cm diameter $\times$ 60 cm height) filled to a depth of 29 cm with opaque water maintained at 24 ± 1°C. A circular transparent acrylic platform (10 cm diameter) was submerged 1 cm below the water surface in a fixed target quadrant. Visual cues were provided inside and outside the maze to facilitate spatial mapping. Each trial began with the mouse in the water facing the tank wall, pseudo-randomly assigned to one of four quadrants. Mice were allowed up to 90 s to locate and mount the hidden platform. Upon successful mounting, mice remained on the platform for 30 s. Animals that failed to locate the platform within the allotted time were gently guided to it and allowed to remain for 30 s to facilitate spatial learning. Mice underwent three daily sessions with 45-min inter-session intervals, over five consecutive training days. Visible platform trials were performed using a red reflective marker to ensure visual acuity and motor coordination. Behavioral tracking was conducted using Noldus EthoVision XT software, which recorded swim path, speed, latency to platform (escape latency), and total distance traveled.

Ultrastructural analysis by transmission electron microscopy (TEM)

For ultrastructural evaluation of the neurovascular unit (NVU), mice were deeply anesthetized and transcardially perfused with a fixative solution containing 15% picric acid (13% saturated solution; Sigma-Aldrich, St. Louis, MO, USA), 4% paraformaldehyde (Electron Microscopy Sciences, Hatfield, PA, USA), and 0.1% glutaraldehyde (EM grade 50% solution; Electron Microscopy Sciences), prepared in a general tubulin buffer (PEM; 0.1 M PIPES, pH 7.2, 1 mM EGTA, 1 mM $MgCl_2$). Brains were rapidly extracted, sectioned coronally, and post-fixed in the same solution for 4 h at 4°C. Samples were processed for transmission electron microscopy (TEM) following established protocols and imaged using JEOL1200EX (JEOL, Tokyo, Japan) with an AMT 2k camera (Advanced microscopy techniques, Woburn, MA).

Quantitative analysis of NVU components

Electron micrographs were acquired from the frontal cortex, specifically targeting a 300 $\times$ 60 μm region containing microvascular profiles. For each experimental group, 10 to 20 discrete NVUs were imaged to assess subcellular integrity, including lumen morphology, basal lamina architecture, endothelial nuclear morphology, and intracellular vacuolations. Quantitative morphometric analysis was conducted in ImageJ, focusing on four parameters: (i) Basement membrane thickness, measured at four cardinal points (3, 6, 9, and 12 o'clock positions) between the inner and outer laminar boundaries while avoiding pericytic expansions; (ii) Lumen circularity ratio, calculated as the longest lumen diameter divided by its perpendicular bisector; (iii) Endothelial vacuolization, defined as the number of cytoplasmic vacuoles >50 nm per 10 μm of endothelial circumference; and (iv) Endothelial nuclear compaction,

quantified as the percentage of NVU profiles containing condensed, electron-dense endothelial nuclei. All image acquisition and analyses were performed under blinded conditions to ensure unbiased quantification across experimental groups.

Whisker stimulation and laser Doppler flowmetry

To assess real-time neurovascular coupling assessment in response to whisker stimulation, mice underwent unilateral whisker stimulation under light anesthesia followed by real-time measurement using laser Doppler flowmetry (LDF). Animals were anesthetized via intraperitoneal injection of ketamine (100 mg/kg) and xylazine (10 mg/kg) and secured in a stereotaxic apparatus. After shaving and disinfecting the scalp, a midline incision was made to expose the intact skull. Care was taken to avoid damaging underlying bone or vasculature. Body temperature was maintained at 37°C with a feedback-controlled heating pad throughout the procedure. LDF probes (moorVMS-LDF or equivalent) were positioned stereotaxically above the right barrel cortex (approximately 1.5 mm posterior and 3.0 mm lateral to bregma), corresponding to the cortical representation of the contralateral whisker pad. Baseline cerebral blood flow (CBF) measurements were recorded for 1 min prior to stimulation. Whisker stimulation was performed for 30 s by mechanically stroking the contralateral vibrissae with a custom-made motorized cell strainer (Corning CLS431750) holder. Simply, the cell strainer is attached to a Vortex Genie, allowing to perform the whisker stimulation at a consistent speed of 3000 rpm. Trials were separated by inter-stimulus intervals of 1 min to enable full vascular recovery, and the procedure was repeated 3 times. Stimulus-evoked changes in CBF were continuously recorded and analyzed as percentage changes from baseline. Peak amplitude, time-to-peak, and recovery kinetics were extracted using vendor software where applicable. All procedures were conducted under blinded conditions per institutional animal care and NIH guidelines.

HPLC-MS/MS analysis of free fatty acids

To assess lipidomic alterations associated with brain injury and dietary modulation, high-performance liquid chromatography coupled with tandem mass spectrometry (HPLC-MS/MS) was employed to quantify free fatty acid (FFA) profiles in serum and cortical tissue.

Blood collection and free fatty acid quantification

Mice were anesthetized under isoflurane, and blood was collected via abdominal vein venipuncture using an insulin syringe. Serum was separated by centrifugation at 4°C, then aliquoted and stored at −80°C until lipid extraction. For all mice, a fixed volume of 100 μL serum was used for FFA extraction and analysis by HPLC-MS/MS with internal standards. Serum FFA concentrations are reported normalized to this fixed volume (pmol per μL serum) to allow consistent comparison across experimental groups and time points.

Brain tissue FFA quantification

Anatomically matched cortical regions were dissected from each animal, with experimental samples taken from a pathologically affected cortical area (~5 mm^3) enriched in tau pathology and estimated to contain ~2.5×10^5 neurons; homologous regions were collected from control mice using the Allen Brain Reference Atlas for spatial consistency. Tissue was homogenized in RIPA buffer and total protein concentration was measured. A fixed aliquot of homogenate was then used for lipid extraction and targeted FFA analysis, performed by the Lipidomics Shared Resource, Analytical Unit using validated protocols. FFA levels were quantified by HPLC-MS/MS and expressed per mg of total protein (pmol/mg protein), a standard practice in tissue-based lipidomics that allows normalization for variability in tissue mass and extraction efficiency. All dissections, processing steps, and mass spectrometric analyses were performed under blinded conditions, and internal standard recovery was monitored across batches to ensure analytical consistency.

Free fatty acid quantification by HPLC–MS/MS

Free fatty acids were quantified at the MUSC Lipidomics Shared Resource using a Thermo Scientific Vanquish UHPLC system coupled to a Thermo Scientific TSQ Quantis Plus triple quadrupole mass spectrometer operated in negative-mode electrospray ionization with selected-ion monitoring. Chromatographic separation was performed on a C18 Peak column (150 × 3.0 mm, 3 μm particle size). Mobile phase A consisted of water containing 2 mM ammonium formate and 0.2% ammonium hydroxide, and mobile phase B consisted of methanol with 1 mM ammonium formate. Analytes were resolved under gradient elution with an approximate total runtime of 30 min. All HPLC–MS/MS analyses were performed using validated workflows established at the MUSC Lipidomics Shared Resource and implemented as previously described.[94–96]

Prior to analysis, serum or tissue homogenate samples underwent liquid–liquid extraction using ethyl acetate:isopropanol following addition of an aqueous ammonium-formate phase. Organic extracts were dried and reconstituted prior to injection according to batch-specific protocols provided by the Lipidomics Core. Quantification was performed using eight-point calibration curves with 1/x weighting, based on analyte-to-internal-standard peak-area ratios. Authentic standards were used for nearly all measured fatty acids; where unavailable, C12:0 was quantified relative to C14:0 and C26:1 relative to C26:0 as defined surrogate calibrators. C17:0-FFA and C23:0-FFA were used as internal standards. Final concentrations were reported in the units specified by the Core for each batch (pmol or nmol, normalized to mass or volume as appropriate), and exact units are indicated in the corresponding figure legends.

Antibodies

The following primary antibodies were used for western blotting and immunohistochemistry: anti–phospho-tau (Ser202/Thr205; AT8, MN1020, Thermo Fisher Scientific), FITC-conjugated Lycopersicon esculentum lectin (LEL 488; DL1174, Vector Laboratories),

anti–collagen type VI alpha 6 (Col6a6; NBP2-14546, Novus Biologicals), anti-agrin (NBP1-90209, Novus Biologicals), anti–collagen type IV alpha 1 (Col4a1; MA5-47009, Invitrogen), Calcein AM Viability Dye (65-0853-39, Invitrogen), anti–VE-cadherin (D87F2; 2500S, Cell Signaling Technology), anti–claudin-5 (35–2500, Invitrogen), anti–peroxisome proliferator-activated receptor alpha (PPARα/NR1C1; NB600-636, Novus Biologicals), anti–matrix metalloproteinase 9 (MMP9; MA5-15886, Invitrogen), anti–β-actin-peroxidase conjugate (A3854, Millipore Sigma), Iba1 (ab178846, Abcam), 4-HNE (ab46545, Abcam) and NeuN (ab104225, Abcam).

Western blotting

Equal amounts of total protein (9 μg per lane) were resolved by SDS-PAGE using 4–12% Bis-Tris polyacrylamide gels and subsequently transferred to nitrocellulose membranes. Membranes were blocked for 1 h at room temperature in either 5% nonfat dry milk or BSA diluted in Tris-buffered saline with 0.1% Tween 20 (TBST), followed by overnight incubation at 4°C with primary antibodies diluted in 5% bovine serum albumin (BSA) in TBST. Target antibodies were used at either a1:1000 or 1:2,000 dilution; β-actin (loading control) was incubated separately at a 1:10,000 dilution. Following primary antibody incubation, membranes were washed with TBST and probed for 1 h at room temperature with species-specific horseradish peroxidase (HRP)–conjugated secondary antibodies (1:5,000 dilution). Prestained molecular weight markers were run in parallel to confirm protein band sizes. Signal detection was performed using enhanced chemiluminescence (ECL) reagents, and membranes were imaged using the Amersham Imager 680 system (GE Healthcare Bio-Sciences, Marlborough, MA, USA). Relative protein expression was quantified by densitometric analysis in QUANTL software and normalized to β-actin expression for each lane.

Immunostaining

Immunofluorescence staining of mouse and human brain sections was performed as previously described, with slight modifications. Tissue sections were first incubated in 0.3% hydrogen peroxide to quench endogenous peroxidase activity, followed by antigen retrieval via brief boiling in 10 mM sodium citrate buffer (pH 6.0). After cooling, sections were blocked with manufacturer-supplied blocking buffer (Invitrogen) and incubated overnight at 4°C with primary antibodies diluted in the same buffer. Signal amplification for single-label immunohistochemistry was performed using biotin-conjugated secondary antibodies (Jackson ImmunoResearch) followed by streptavidin–horseradish peroxidase (HRP; Invitrogen). For double immunofluorescence labeling, Alexa Fluor 488– or Alexa Fluor 568–conjugated isotype-specific secondary antibodies (Jackson ImmunoResearch, West Grove, PA, USA) were applied for 1 h at room temperature. Sections were washed four times with Tris-buffered saline (TBS) between each step. Immunolabeled samples were imaged using a Zeiss laser-scanning confocal microscope or Keyence Microscope BZ-X series. Laser gain and offset were optimized based on negative control sections lacking primary antibodies, ensuring no autofluorescence or background signal contributed to image capture. Identical acquisition parameters were used across experimental groups. Images were analyzed using Volocity 6.3 software (PerkinElmer) and Fiji/ImageJ Coloc 2 plugin to quantify fluorescence intensity and co-localization. Three-dimensional reconstruction and volumetric analyses were performed in Imaris (Bitplane). z stack images were imported into Imaris (Oxford Instruments) for quantification of surface rendering, signal segmentation, and colocalization. Regions of interest were defined manually or semi-automatically using intensity-based thresholding and surface creation tools. Quantitative morphometric parameters such as object volume, surface area, and spatial proximity were extracted. Rendering and post-processing were conducted under blinded conditions to ensure objectivity in image interpretation.

Transcriptomic profiling and weighted gene Co-expression network analysis (WGCNA)

Total RNA was extracted from injured cortical tissue using the RNeasy Mini Kit (Qiagen) according to the manufacturer's protocol. RNA integrity was assessed using the Agilent 2100 Bioanalyzer, and only samples with RNA integrity numbers (RIN) $\geq$8.0 were included for downstream analysis. RNA concentrations were quantified using the Qubit RNA HS Assay Kit (Invitrogen). Library preparation was performed using the NEBNext Ultra II RNA Library Prep Kit (New England Biolabs), followed by sequencing on an Illumina NovaSeq 6000 platform to generate 150-bp paired-end reads with an average depth of ~40 million reads per sample. Raw sequencing reads were quality-checked using FastQC and trimmed with Trimmomatic to remove adapter sequences and low-quality bases. High-quality reads were aligned to the mouse reference genome (GRCm38/mm10) using STAR aligner. Read counts were generated using HTSeq-count, and gene expression matrices were normalized via variance-stabilizing transformation (VST) using the DESeq2 package in R. Weighted Gene Co-expression Network Analysis (WGCNA) was performed on normalized expression data to identify gene modules associated with dietary treatment and TBI status. Genes with low variance across samples were filtered out, retaining the top 75th percentile of expressed genes. An unsigned gene co-expression network was constructed using the WGCNA package in R (v1.70-3). Based on scale-free topology criteria, a soft-thresholding power was selected (typically β = 6–10). Topological overlap matrices (TOMs) were computed to define network connectivity, and hierarchical clustering was used to identify modules of co-expressed genes (minimum module size = 30). Modules were assigned unique color identifiers for downstream tracking. For each module, the eigengene (ME) corresponding to the first principal component of a given module was calculated. Intramodular hub genes were identified based on module membership (kME >0.8) and gene significance scores. Gene ontology (GO) enrichment analysis and KEGG pathway mapping were performed for key modules using clusterProfiler and g:Profiler to determine biological processes and signaling pathways enriched in the co-expression modules of interest. All analyses were performed in R (v4.2.2) with integrated graphical outputs produced using ggplot2 and Cytoscape (v3.9) for network visualization.

Quantitative real-time PCR (qRT-PCR)

Candidate genes identified through weighted gene co-expression network analysis (WGCNA) were validated by quantitative real-time PCR (qRT-PCR) using total RNA extracted from the injured cortex of mice (n = 5 per group) and the superior frontal cortex of human postmortem samples. RNA was isolated with the RNeasy Mini Kit (Qiagen), treated with DNase I, and assessed for purity and integrity using NanoDrop spectrophotometry and Agilent Bioanalyzer. cDNA synthesis was performed with the High-Capacity cDNA Reverse Transcription Kit (Applied Biosystems), and gene expression levels were quantified using pre-designed TaqMan Gene Expression Assays (Applied Biosystems) on a QuantStudio 6 Flex Real-Time PCR System or a LightCycler 480 II PCR machine (Roche). For SYBR Green–based detection, qPCR reactions were carried out using LightCycler 480 SYBR Green I Master Mix (Roche) under a two-step protocol: initial denaturation at 98°C for 2 min, followed by 40 cycles of 95°C for 5 s and 58°C for 30 s. Each sample was run in triplicate, and relative mRNA expression was calculated using the $2^{-\Delta\Delta Ct}$ method. GAPDH was used as the endogenous reference gene (Mouse: Gapdh, Assay ID Mm99999915_g1; Human: GAPDH, Assay ID Hs99999905_m1), with vehicle-treated samples serving as the reference baseline for ΔΔCt calculations. The following gene-specific assay IDs were used: mouse – Claudin 5 (Mm00727012_s1), Eng (Mm00468252_m1), PPARα (Mm00440939_m1); human – PPARα (Hs00231882_m1), LRP4 (Hs00391006_m1), ELOVL7 (Hs04400799_m1), COL8A1 (Hs00156669_m1). All reactions demonstrated optimal amplification efficiencies (90–110%), and specificity was confirmed via melting curve analysis and the absence of nonspecific amplification. Gene-specific primers are listed (ORIGENE) in Figure S4.

In vitro assays

For *in vitro* treatment studies, HBEC-5i cells were seeded into gelatin-coated multiwell plates and exposed to one of the following media formulations: (1) control medium (VEC:M199 with 5% FBS), (2) control medium supplemented with 100 μM AICAR (5-Aminoimidazole-4-carboxamide ribonucleotide) and 50 μM L-carnitine, (3) control medium with 100 μM eicosapentaenoic acid (EPA; Sigma-Aldrich), or (4) EPA replacement with 100 μM docosahexaenoic acid (DHA; Sigma-Aldrich), co-administered with AICAR (100 μM) and L-carnitine (50 μM). EPA and DHA were pre-complexed with bovine serum albumin (BSA) at a 2:1 molar ratio prior to administration to ensure bioavailability and reduce oxidation. Cells were exposed to treatment conditions for specified durations depending on the downstream assay (e.g., viability, migration, TEER, or angiogenic tube formation). All experiments were performed using cells within 10 passages from thawing to preserve endothelial phenotype.

Preparation of fatty Acid–BSA conjugates (EPA and DHA)

To prepare physiologically relevant, water-soluble fatty acid solutions for *in vitro* studies, long-chain fatty acids, EPA and DHA, were conjugated to fatty acid–free BSA at a 6:1 molar ratio (fatty acid:BSA). Fatty acid–BSA complexes were freshly prepared before each experiment to ensure stability and bioavailability.

I. Preparation of BSA Solution: Ultra fatty acid–free BSA (2.267 g) was dissolved in 100 mL of 150 mM NaCl solution in a pre-warmed 250 mL beaker containing a stir bar. The beaker was sealed with parafilm and placed in a 1 L water bath maintained at 37°C (not exceeding 40°C) while stirring until fully dissolved. The solution was sterile-filtered through a 0.22 μm vacuum filtration unit under laminar flow. After filtration, 50 mL was transferred to a pre-warmed 250 mL beaker for immediate use, while the remaining 50 mL was diluted 1:1 with an additional 150 mM NaCl to create a 0.17 mM BSA stock solution, which was aliquoted (4 mL/vial) and stored at −20°C for use as vehicle control.
II. EPA and DHA–BSA Conjugation: EPA and DHA (≥98% purity; Sigma-Aldrich) were first dissolved in 100% ethanol to generate 50 mM stock solutions, stored in amber vials under nitrogen gas at −80°C. For conjugation, the fatty acids were diluted into the pre-warmed 2% fatty acid–free BSA solution in endothelial culture medium to achieve a final concentration of 100 μM EPA or DHA and 0.5% BSA (w/v). The mixture was vortexed and incubated at 37°C for 30 min with gentle stirring. The solution was then filtered through a 0.22 μm syringe filter and used immediately for cell treatment. All fatty acid–BSA preparations were protected from light, prepared fresh or thawed on the day of use, and never subjected to repeated freeze-thaw cycles.

Tube formation assay

To assess angiogenic capacity, growth factor–reduced Matrigel (Corning 354230) was added (200 μL/well) to 24-well plates and allowed to polymerize at 37°C for 1 h. HBEC-5i cells (4×10^5/well) were seeded on Matrigel under the specified treatment conditions. Tube formation was monitored over time, and after 18 h of incubation, the media were gently refreshed with the same respective treatments to sustain viability and structural integrity. Cells were incubated for an additional 18 h (total incubation time: 36 h). After 36 h, tube-like structures were stained with Calcein-AM (2 μM, Invitrogen) and imaged using a Keyence BZ-X800 fluorescence microscope. ImageJ with the Angiogenesis Analyzer plugin was used to quantify nodes, junctions, meshes, and segments. Experiments were performed in triplicate under blinded conditions.

Electric Cell-Substrate Impedance Sensing (ECIS) wound healing assay

Confluent HBEC-5i monolayers in 96W1E + ECIS arrays were electrically wounded (3,000 μA at 60,000 Hz for 60 s). Migration into the denuded area was tracked via impedance recovery at 4,000 Hz over 24 h. Data were analyzed using ECIS software and plotted as impedance recovery curves.

Transepithelial/transendothelial electrical resistance (TEER) mesaurements

Barrier integrity was measured using Electric Cell-Substrate Impedance Sensing (ECIS; Applied BioPhysics, Zθ system). HBEC-5i cells were seeded in 96W1E + ECIS arrays at 5,000 cells/well. TEER was recorded at 4,000 Hz once daily for five consecutive days. Readings were normalized to blank wells. All conditions were measured in triplicate.

MTT assay for cell viability

HBEC-5i cells (5,000/well) were seeded in 96-well plates and treated for 1 or 3 days. On assay days, MTT (0.5 mg/mL in PBS) was added and incubated at 37°C for 3 h. Formazan was solubilized with DMSO, and absorbance was read at 570 nm. Each condition was tested in eight technical replicates, with three independent experiments performed.

In silico target prediction of EPA and DHA

To explore potential molecular targets of the omega-3 polyunsaturated fatty acids eicosapentaenoic acid (EPA) and docosahexaenoic acid (DHA), an *in-silico* target prediction analysis was conducted using the SwissTargetPrediction platform (https://www.swisstargetprediction.ch/). Canonical SMILES (Simplified Molecular Input Line Entry System) representations of EPA (PubChem CID: 446284) and DHA (PubChem CID: 445580) were retrieved from the PubChem Compound Database (https://pubchem.ncbi.nlm.nih.gov/). These structures were submitted to the SwissTargetPrediction tool, which employs 2D and 3D molecular similarity measures to infer probable macromolecular targets based on known ligand-target interactions in the ChEMBL database. Predictions were performed for the Homo sapiens species, and the output included a ranked list of putative targets with associated probability scores, functional classes (e.g., nuclear receptors, enzymes, membrane receptors), and mechanistic annotations. This computational approach allowed for the systematic identification of protein targets potentially modulated by EPA and DHA, supporting further hypotheses regarding their roles in neurovascular regulation and metabolic signaling pathways. Target prediction results were used to complement transcriptomic and proteomic findings and to inform pathway enrichment and druggability analyses.

QUANTIFICATION AND STATISTICAL ANALYSIS

All data were analyzed using GraphPad Prism (v10.0; GraphPad Software, San Diego, CA, USA) and R statistical environment (v4.2.2). Normality of distribution was assessed using the Shapiro–Wilk test and Q–Q plots. For comparisons between two groups, unpaired two-tailed Student's t-tests were used for normally distributed data, while Mann–Whitney U tests were applied for non-parametric comparisons. For multi-group comparisons, one-way or two-way ANOVA with appropriate post hoc corrections (Tukey's, Sidak's, or Dunnett's) were used depending on the experimental design. Repeated-measures ANOVA was applied to analyze time-course data including TEER, wound healing, ECIS impedance recovery, and behavioral performance across multiple time points. Statistical significance for all ANOVA models was verified by Greenhouse–Geisser correction when the assumption of sphericity was violated. For transcriptomic data, differential gene expression analysis was performed using the DESeq2 package, and p-values were adjusted for multiple testing using the Benjamini–Hochberg false discovery rate (FDR) correction. Co-expression network modules identified via WGCNA were correlated with experimental phenotypes using Pearson's correlation coefficient, and hub genes were defined by high module membership (kME >0.8) and gene significance scores (GS > 0.5). Gene ontology and pathway enrichment analyses were performed using hypergeometric testing and corrected for multiple comparisons. All *in vitro* experiments were performed with a minimum of three biological replicates and 6–8 technical replicates per condition unless otherwise stated. *In vivo* sample sizes were determined based on prior power calculations ($\alpha = 0.05$, $\beta = 0.2$, power = 0.8) derived from pilot data to detect a $\geq$20% change with a standard deviation of 15%. Outliers were identified using Grubbs' test and excluded only if attributable to technical error. Data are expressed as mean ± standard error of the mean (SEM), and statistical significance was set at $p < 0.05$. All analyses were performed under blinded conditions to ensure unbiased assessment across experimental groups. Statistical significance is indicated in figures as NS (not significant) or by asterisks: $^{*}p < 0.05$, $^{**}p < 0.01$, $^{***}p < 0.001$, $^{****}p < 0.0001$. Unless otherwise stated in the figure legends, two group comparisons used an unpaired two-tailed Student's t test (or Mann-Whitney U test for non-parametric data), and multi-group comparisons used one-way or two-way ANOVA with Tukey's, Sidak's, or Dunnett's multiple comparisons post hoc tests as appropriate.